Identification of the influential DEM contact law parameters on powder bed quality and flow in additive manufacturing configurations

Maxime Stephan, Guilhem Roux, Alexis Burr, Carine Ablitzer, Jean-Paul Garandet

Graphical Abstract

Identification of the influential DEM contact law parameters on powder bed quality and flow in additive manufacturing configurations

Maxime Stephan, Guilhem Roux, Alexis Burr, Carine Ablitzer, Jean-Paul Garandet

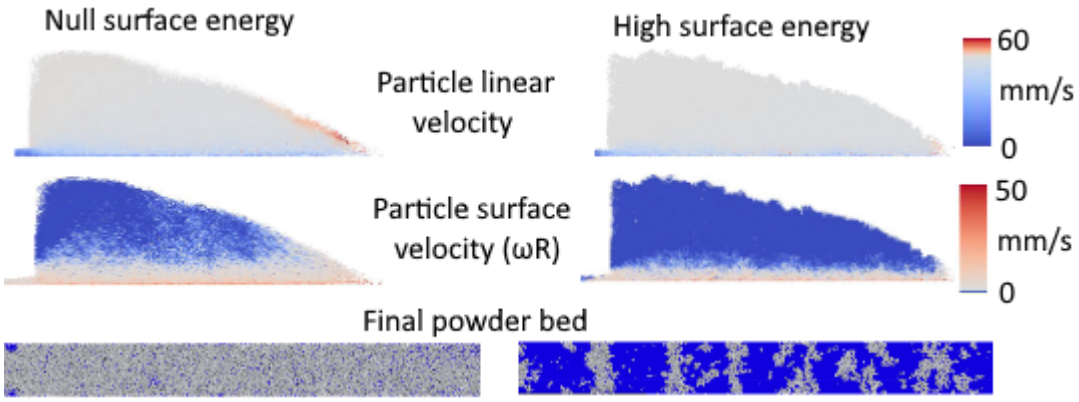

Highlights

Identification of the influential DEM contact law parameters on powder bed quality and flow in additive manufacturing configurations

Maxime Stephan, Guilhem Roux, Alexis Burr, Carine Ablitzer, Jean-Paul Garandet

- Effective surface energy between powder particles is a key parameter to assess bed-forming ability.
- Rolling friction between particles also contributes significantly to powder bed quality.
- A sliding friction above 0.4 is required to counter powder resistance and ensure deposition.
- The heap profile ahead of the blade can be a good predictor of powder spreadability.
- The observed size segregation on the fabrication plate can be traced to powder motion during the feeding stage.

Identification of the influential DEM contact law parameters on powder bed quality and flow in additive manufacturing configurations

Maxime Stephan[a], Guilhem Roux[a], Alexis Burr[a], Carine Ablitzer[b], Jean-Paul Garandet[a]

[a] *Univ. Grenoble Alpes, CEA, LITEN, DTNM, L3M, Grenoble, 38000, France*
[b] *CEA, DES, IRESNE, DEC, Cadarache, Saint-Paul-lez-Durance, 13108, France*

Abstract

The main objective of the present manuscript is to implement DEM simulations of powder spreading in an Additive Manufacturing process. A numerical sensitivity analysis is carried out in order to identify the contact law parameters that impact most on powder bed quality. Tested parameters are surface energy, as well as sliding, rolling and restitution coefficients. It is seen that effective surface energy between powder particles is a key parameter to assess bed-forming ability, but that it is also necessary to consider rolling and sliding frictions for an accurate modeling of the spreading phenomena. In addition, our simulations allow a better understanding of the size segregation issues during the feeding and deposition stages. Finally, we describe the effect of the contact law parameters on the heap profile. We identify various powder flow zones within the heap, and show that heap profile can be a predictor of powder bed quality.

Keywords: Powder Spreading, Discrete Element Method, Contact Law, Adhesion, Sliding Friction, Rolling Friction

1. Introduction

A number of Additive Manufacturing (AM) processes (e.g. Powder bed fusion (PBF) and Metal Binder Jetting (MBJ)) are manufacturing processes that allow the production of metallic parts from powder by successive spreading and densification of powder layers. Other materials can be also used in powder bed based AM techniques, such as polymers with Selective Laser Sintering (SLS) or Multi Jet Fusion (MJF). All those processes enable the production of complex shapes, making them useful for a variety of applications. The first critical step in powder bed based AM processes is powder spreading, which is commonly assumed to lead to denser and smoother surfaces of the final parts if it is even and homogeneous [1]. Powder paving marks the initial state before heat densification in the case of PBF or binder absorption in the case of MBJ [2, 3]. For L-PBF (Laser-PBF), powder layer quality is critical for final part density only in case of packing density under a certain threshold [4]. Even if the gas flow around laser beam and melt pool leads to denudation of the powder layer along the laser path, passage through the liquid state allows to some extent a smoothing of the density variations. However, large empty patches and inhomogeneities can not be corrected by fusion [5, 6]. Moreover, powder bed roughness is correlated with final L-PBF part roughness [4]. In MBJ, the shrinkage during sintering largely depends on the distribution of the green part porosity. Therefore, the achievement of a homogeneous bed is of paramount importance as variations in porosity between layers may cause distortions of the final printed part. Even more important, as opposed to the case of fusion, low densities and inhomogeneities can not be corrected by sintering. On the other hand, excessive densities makes binder absorption more difficult, which makes green parts brittle and harder to handle [3]. Therefore, an optimal bed density is a compromise between the possibility of reaching a large density after sintering and the capacity for binder absorption

within the bed.

The spreading mechanisms depend on powder characteristics, such as powder morphology and size distribution. An a priori counterintuitive fact is that powder flowability measured with dedicated qualification equipment is not necessarily correlated with powder spreadability during process [1, 7, 8]. From a general standpoint, a water atomized powder-spreading results in low packing density and high layer roughness, because of the low particle sphericity [9]. In addition, a powder with a wide Particle Size Distribution (PSD) can be beneficial for adequate layer formation. For bimodal distribution, a small amount of fine particles has a positive effect on bed density and smoothness as it allows filling of the voids within the bed. However, over a certain fraction of small particles Van der Waals forces become too important, leading to particle agglomeration and a poor powder bed quality [7]. In principle, an optimal fine fraction can be identified, depending on the original powder PSD [3].

The geometry of the spreading device can have a significant impact on powder bed quality. Rollers based on counter-rotating movement allow particles to rearrange; however, they increase particle segregation and require a minimum spreading height, typically over 1.8xD90, D90 representing the 90th volume-percentile of the considered powder [10]. An increased roller diameter results in a larger compression force on the powder bed [11]. Concerning metallic scrapers, an angle of attack between 5° and 15° allows an appropriate compaction [12]. Haeri [13] simulated an elliptic blade profile, and obtained better results than with a roller. According to Wang et al.[14], a round blade gives a better performance than rollers and angled blades. From a process standpoint, the main parameters that can be optimized are the nominal spreading height and spreading device velocity. Indeed, the largest particles of a distribution (typically over the D90) fix the minimum layer thickness [9]. Moreover, an increase of the nom-

inal height and a reduction of the spreading speed lead to denser and smoother powder bed [15]. However, in L-PBF the actual spreading height is often far away from the nominal spreading height set by the machine user. A first factor accounting for such a difference is powder densification upon melting. Actual spreading height values increase during the first layers. Then, a steady state is reached after about ten layers [16, 17]. Nominal height and spreader velocity can also contribute to this difference.

An optimization of the powder bed quality can be achieved through a numerical simulation of the spreading process. The Discrete Element Method (DEM) (see e.g. [18]) allows a mathematical representation of the dynamic behavior of a set of particles where each powder particle is considered independently, their motions being derived from the integration of Newton's law. It thus allows the modeling of powder spreading and the investigation of physical phenomena such as powder flow dynamics and force arches [10, 17, 19]. A common characteristic feature of DEM modeling is that the shape of the particles is assumed spherical, the constitutive contact laws being expressed on the basis of a theoretical interpenetration [18]. All the interactions between particles are expressed through those contact laws. The technique has been widely used to model powder bed formation in additive manufacturing configurations [14, 15, 19–21].

During spreading, a powder heap can be observed in front of the blade. Previous works have highlighted different heap zones in terms of flow behavior. Avalanche or free-flowing zone is observed close to the upper part, specially near the front of the powder heap [10, 20], whose shape farthest away from the blade can be characterized by a Recoating Angle (RA) [20, 22] also called Dynamic Repose Angle [23, 24]. Just over the plate, a deceleration zone contains the particles that are slowed down due to the effect of plate friction. Over this deceleration zone, a quasi-static or slow flow zone [10] covers the majority of the

heap and is characterized by an almost zero particle velocity in the blade frame. Finally, in the vicinity of the blade gap with the plate, a shear stress region contains force arches that partially govern effective powder deposition [17, 20].

A complexity of the DEM technique is that, depending on the contact law implemented, a large number of parameters are often necessary as inputs in the simulation. For example, the Hertz-Mindlin contact with Johnson Kendall Roberts (JKR) adhesion model requires no less than 6 parameters, namely Young's modulus, Poisson's ratio, effective surface energy, restitution coefficient, and then sliding and rolling friction coefficients [25–27]. Moreover, in powder spreading simulations, contact parameters between powder particles, powder and the plate as well as powder and the blade are expected to be different.

Whenever possible, it is of course preferable to independently measure the constitutive parameters through the design of specific experiments that can be interpreted on a physical basis. An example is the drop test method for effective surface energy [28]. Another approach is based on calibration by flow experiments and macroscopic metrics. However, the number of necessary parameters is such that a priori assumptions on the physical phenomena to account for are necessary. Many routines of calibration are proposed in the literature, essentially based on packing density, and static and dynamic Angle of Repose (AOR) [20, 29, 30]. The use of a powder rheometer with shear cell or impeller blade is also possible [31, 32]. Choice of calibration experiments must feature dynamic and static behavior in order to cover various powder flow aspects, as static and dynamic Angle of Repose [1, 20].

The main objective of the present manuscript is to carry out a numerical sensitivity analysis in order to determine contact law parameters that have the greatest impact on powder bed quality. Tested parameters are effective surface energy, restitution coefficient, and sliding and rolling friction coefficients.

Here a particular attention is paid to the discrimination between the various types of contact frictions, namely *powder/powder*, *powder/building plate* and *powder/spreading blade*. Indeed, because of different surface characteristics between particles and bulk material it appears necessary to address this point in detail. Regarding the *powder/spreading blade* contact, it is expected to be very much geometry dependent [13, 29], and would require a dedicated analysis, which is outside the scope of the present manuscript. On the other hand, there is a lack of knowledge about *powder/plate* interaction; therefore, focus will be on this issue. The second objective of our work is to describe the effect of the contact law parameters on the heap profile, through an in-depth analysis of slope angle measurements. Thanks to particle velocity and rotation, flow zones within the heap can be identified. Then, powder flowability and plate friction can be linked to powder flow, heap profile and finally powder bed quality.

The modeled powder is a thin 316L stainless steel metallic powder commonly used in L-PBF. To carry out the proposed objectives, we decided to focus on a simple fixed geometry set-up, thus allowing the implementation of a large number of numerical simulations with many contact law parameter sets. A powder bed analysis routine is used to post-process raw DEM data. The powder bed quality will be characterized in terms of height, density and their variations along the spreading direction. Particle size segregation is also investigated. Then, contact law parameters are discussed in term of variation ranges and associated powder physical properties. Finally, the effect of contact law parameters are presented within a global analysis of particle movement allowed by DEM data to gain some insights on the effect of these contact parameters on powder flow dynamics.

Nomenclature (SI units are used here, relevant prefixes (milli, micro...) have been used in the text)

DEM calculation and contact laws :

m_i	kg	Mass of a particle i
$\vec{x_i}$	m	Position of a particle i
$\vec{F_i}$	N	Sum of forces acting on a particle i
t	s	Time
I_i	$\mathrm{kg\,m^2}$	Moment of inertia of a particle i
$\vec{\omega_i}$	rad/s	Angular velocity of a particle i
$\vec{M_i}$	$\mathrm{kg\,m^2/s^2}$	Sum of moments acting on a particle i
$\vec{F_n}$	N	Contact normal force between two particles i and j
E	Pa	Young's modulus
ν	dimensionless	Poisson's ratio
R_i	m	Radius of a particle i
δ_n	m	Overlap for a contact between two particles i and j
γ	$\mathrm{J/m^2}$	Effective surface energy
η	kg/s	Damping factor
e	dimensionless	Restitution coefficient
$\vec{F_t}$	N	Tangential force at a contact between two particles i and j
$\vec{\delta_t}$	m	Tangential relative displacement for a contact between two particles i and j
G	Pa	Shear modulus
μ_{sl}	dimensionless	Sliding friction coefficient of a contact between two particles i and j
$\vec{M_{\mathrm{ro}}}$	N m	Moment due to rolling resistance for a contact between two particles i and j

μ_{ro}	dimensionless	Rolling friction coefficient of a contact between two particles i and j
g	m/s^2	External acceleration (gravity)
ρ	kg/m^3	Density
Contact types for $\mu_{\mathbf{sl}}$ and $\mu_{\mathbf{ro}}$:		
po/po		Contacts between powder particles
po/pl		Contacts between powder particles and plates (feeding and building)
all		All contacts : *po/po*, *po/pl* then contacts between powder and blade
Simulation condition :		
L	m	Length along x axis, blade moving direction
W	m	Width along y axis, direction normal to periodic boundaries
H	m	Height along z axis, direction of the gravity
Δt	s	Time step
v	m/s	Velocity (blade)
Contact law parameters illustration :		
$\overrightarrow{F_{n,\text{pull-off}}}$	N	Pull off force due to JKR adhesion term [27]
n_s	dimensionless	Sides of a polygon (Estrada theory [33])
Results characterization		
a	m	Grid parameter
$\bar{H}$	m	Mean height of powder bed
$\bar{\varphi}$	dimensionless	Mean relative powder bed density
D_{43}	m	Volume moment mean diameter
$\mathrm{RA}_{\mathrm{attack}}$	rad	Recoating Angle (front of heap)

RA_{HL}	rad	Recoating Angle (Global on heap)
$\vec{v}$	m/s	Linear velocity (particle)
$\vec{v_s}$	m/s	Surface velocity (particle)

2. Methodology

2.1. Discrete Element Method, contact laws

MUSEN is a DEM open-source software used for numerical simulation. It allows GPU computation saving time compared to CPU computation [34]. Each particle i is spherical and defined by its position $\vec{x_i}$ and angular velocity $\vec{\omega_i}$. At each time step Δt, those values are updated from the sum of forces $\vec{F_i}$ and moments $\vec{M_i}$ acting on each particle i [35]:

$$m_i \frac{d^2\vec{x_i}}{dt^2} = \vec{F_i}, \qquad I_i \frac{d\vec{\omega_i}}{dt} = \vec{M_i} \tag{1}$$

m_i, I_i are the mass and moment of inertia of the particle i. Forces $\vec{F_i}$ and moments $\vec{M_i}$ result from contacts with walls or particles and gravity. Contact laws are used to compute all of the interactions between particles and between particles and surfaces.

The resulting normal contact force on particle i takes into account an elastic repulsion with damping; it is calculated using Hertz-Mindlin contact law [25, 26]. Following Johnson, Kendall, and Roberts, [27], thereafter referred to as JKR, an additional adhesion term is considered:

$$\vec{F_n} = \left(-\frac{4\sqrt{R^*{\delta_n}^3}E^*}{3} + \sqrt{8\pi E^* \gamma \sqrt{{\delta_n}^3 {R^*}^3}} - \eta_n \dot{\delta_n} \right) \vec{n} \tag{2}$$

E^* and R^* are the equivalent Young's modulus and equivalent radius of the considered contact. Table 1 gives the formulae for equivalent quantities. δ_n is the normal overlap, γ is the effective surface energy of decohesion between two

particles [18] and η_n is the normal damping factor, defined from the restitution coefficient e :

$$\eta_n = \frac{1.8257 \ln(e)}{\sqrt{\pi^2 + \ln^2(e)}} \sqrt{2m^* E^* \sqrt{R^* \delta_n}} \tag{3}$$

e is the ratio between particle velocity after and before a collision ($= v/v_0$). m^* is the equivalent mass. The Hertz-Mindlin model is also used to calculate tangential force at the contact. Tangential contact is elastic with damping until a sliding limit given by Coulomb law:

$$\begin{cases} \vec{F_t} = -8G^* \sqrt{R^* \delta_n} \vec{\delta_t} - \eta_t \dot{\vec{\delta}}_t \\ \text{if} \quad |\vec{F_t}| > \mu_{\text{sl}} |\vec{F_n}| \quad \text{then} \quad \vec{F_t} = \mu_{\text{sl}} |\vec{F_n}| \dfrac{\vec{F_t}}{|\vec{F_t}|} \end{cases} \tag{4}$$

$\vec{\delta_t}$ is the tangential relative displacement, G^* is the equivalent shear modulus, μ_{sl} is the sliding friction coefficient. Then, η_t is the tangential damping factor calculated from e :

$$\eta_t = \frac{3.6514 \ln(e)}{\sqrt{\pi^2 + \ln^2(e)}} \sqrt{2G^* m^* \sqrt{R^* \delta_n}} \tag{5}$$

Rolling friction generates a moment against angular velocity. It is dependent on the contact normal force and the rolling friction coefficient μ_{ro} :

$$\vec{M_{\text{ro}}} = -\mu_{\text{ro}} |\vec{F_n}| R_i \frac{\vec{\omega_i}}{|\vec{\omega_i}|} \tag{6}$$

Then, F_i and M_i introduced in Eq. (1) can be deduced from Eqs. (2),(4) and (6) summing over all contacts with neighbor particles j.

$$\begin{cases} \vec{F_i} = \sum_j (\vec{F_n} + \vec{F_t}) + m_i \vec{g} \\ \vec{M_i} = \sum_j (\vec{M_{\text{ro}}} - R_i \vec{F_t} \wedge \vec{n}) \end{cases} \tag{7}$$

Table 1. Expressions used to calculate equivalent quantities for a contact between two particles i and j.

Quantity	Expression
Equivalent Young's modulus	$E^* = \left(\frac{1-\nu_i^2}{E_i} + \frac{1-\nu_j^2}{E_j}\right)^{-1}$
Equivalent contact radius	$R^* = R_i R_j/(R_i + R_j)$
Equivalent mass	$m^* = m_i m_j/(m_i + m_j)$
Shear modulus	$G_i = E_i/(2(1+\nu_i))$
Equivalent shear modulus	$G^* = \left(\frac{2-\nu_i}{G_i} + \frac{2-\nu_j}{G_j}\right)^{-1}$

2.2. Simulation conditions

2.2.1. Powder supply

Even though no experimental work is reported within the present work, it appeared a priori interesting to model an actual commercial powder commonly used in L-PBF practice and to use measured characteristics as input for the simulations. In this study, a gas atomized (GA) 316L stainless steel powder provided by Sandvik is therefore modeled. The volume-based powder size distribution (PSD) is measured by laser diffraction in ethanol following the ISO 13320 standard (Mastersizer 2000 Malvern®). Volumetric D10, D50 and D90 are equal to **10/18/32** µm respectively. SPAN = (D90-D10)/D50 is equal to **1.2** [36]. The volume-based distribution in the form of size classes is converted to number-based distribution, as shown in Fig. 1.

2.2.2. Geometry

Simulation set-up at different stages is illustrated in Fig. 2. Table 2 provides the different geometrical dimensions and values related to simulation setup. An external acceleration g corresponding to gravity is set to 9.81 $\mathrm{m\,s^{-2}}$ along z-axis. W_{periodic} is the distance between periodic boundaries. It is set as 10 times the size of the D99.5, which is the diameter of the 0.5% largest particles in volume

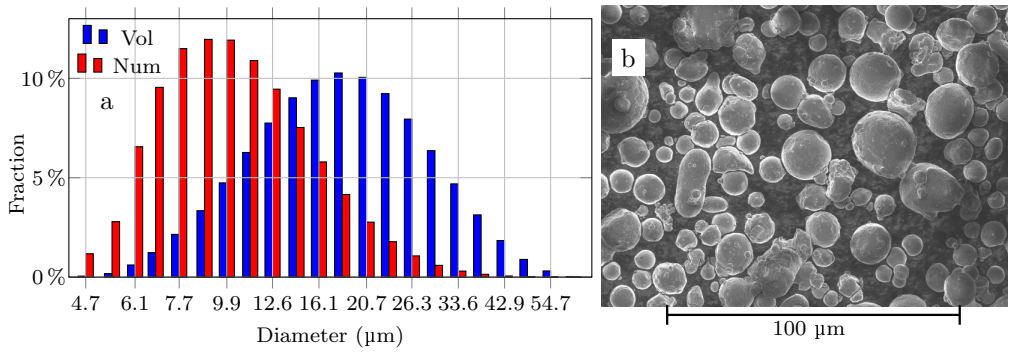

Fig. 1. Powder supply : (a) Volume and number based Powder Size Distribution (PSD) and (b) powder observed by SEM (secondary electrons)

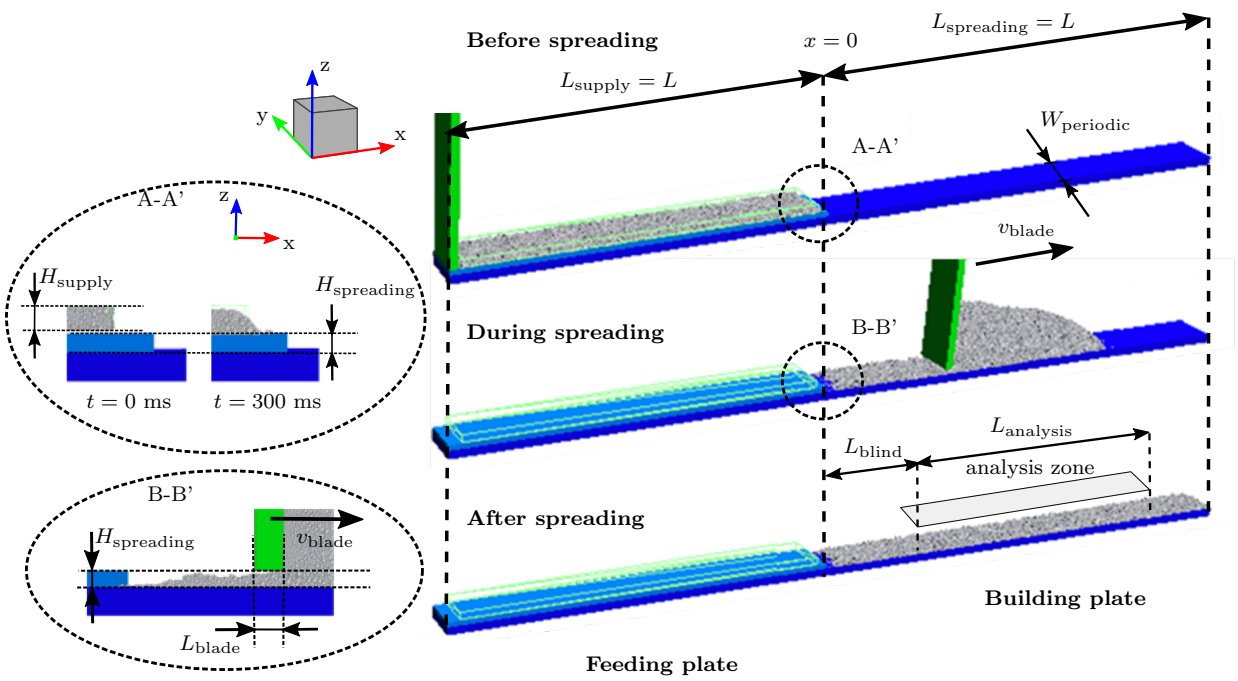

Fig. 2. Spreading simulation geometry at different stages, at t = 0 ms, t = 750 ms and t = 1 s. x-axis length is cut to help representation. A-A' and B-B' zooms show the transition between both plates

Table 2. Spreading simulation dimensions and fixed parameters.

Dimensions	Value
$L_{\text{supply}} = L_{\text{spreading}} = L$ (mm)	15
W_{periodic} (µm)	500
V_{blade} (µm/s)	50
L_{blind} (mm)	4
L_{analysis} (mm)	9
H_{supply} (µm)	90
$H_{\text{spreading}}$ (µm)	60
L_{blade} (µm)	100
g ($\text{m}\,\text{s}^{-2}$)	9.81
Δt (ns)	8

[7, 12, 19]. The spreading length L is set to 15 mm. Such a spreading length is small compared to a real building plate. However, the simulation of a 10 cm-long spreading would require too much computing resources. In order to investigate spreading length effect, one spreading is done with reference powder parameters (introduced in section 2.3.5) and twice the reference length, i.e. 30 mm. As visible in Fig. 2(B-B'), the step between feeding and building plate influences results at the beginning of the bed, therefore the analysis zone starts at a distance L_{blind} from the feeding plate. It allows skipping the first millimeters, where transients in the spreading flow could be observed. The rectangular blade has a thickness L_{blade} of 100 µm. As mentioned earlier, the focus of the present work is not on *powder/blade* interactions; therefore, it was decided to use a generic blade geometry in all simulations.

Initial powder generation takes place in a 90 µm high box slightly raised over the feeding plate in order to avoid interactions with walls at the first time step. First, particles are randomly packed setting a 50% porosity inside the box with the specified PSD. At t=0 particles are released and left to settle on the feeding

plate. The small initial drop and a 300 ms rest time before blade movement allows an equilibrium state to be reached with respect to gravity [15]. After complete spreading, the simulation continues for 100 ms to allow the powder bed to settle. Unless specified otherwise, the material parameters of the blade and the plate are the same as powder particles.

Spreading height $H_{\text{spreading}}$ is set to 60 µm, a value typical of L-PBF processes that is approximately two times the D90 of powder; however, some rare particles (0.03% in volume) are larger than the gap. Depending on the initial bed porosity, laser densification on such a 60 µm layer should result in a final solidified layer of 20-30 µm. In an actual L-PBF process, after few layers (5 to 10), the solidified thickness would approach the spreading height [16]. Therefore, our choice of $H_{\text{spreading}}$ set to 60 µm allows typical values relevant for the L-PBF processes to be covered, both in transient and steady state modes. Blade velocity is fixed to 50 mm/s, again a typical value for L-PBF processes.

2.2.3. Time step and fixed powder parameters

Time step is set to the value recommended by MUSEN [34], which is 10% of the smallest Rayleigh time for the considered particle distribution. Rayleigh time is defined as the time needed for a shear wave to propagate though a solid particle [37, 38]. It can be calculated as a function of the Young's modulus, density, Poisson ratio and particle radius:

$$\Delta t = 0.1 * min \left\{ \frac{\pi * R_i * \sqrt{2\rho(1+\nu_i)}}{\sqrt{E_i}(0.163\nu_i + 0.8766)} \right\} \tag{8}$$

Let us recall that simulated powder consists of perfect spherical particles, with a PSD in number given in Fig. 1. Since Young's Modulus, density and Poisson ratio are well known materials properties, 316L alloy standard values are used for our simulation and fixed [19]. However, for simulation purposes,

Young's Modulus can be decreased by some orders of magnitude in order to increase the time step and so decrease computational time. Based on Chen et al. work [39], Young's modulus is decreased by 3 orders of magnitude. Even at this reduced value, it still complies with the standard criterion on maximal relative overlap over all particles at each time step [38]:

$$\frac{max(\delta_{n,i})}{2R_i} < 0.01 \tag{9}$$

The other option for time step increase, namely material density increase, is not possible in our present spreading configuration, as the particle flow can not be considered quasi-static [18].

2.3. Studied powder contact law parameters

As opposed to the macroscopic parameters discussed just above, the values of effective surface energy, restitution coefficient, as well as sliding and rolling coefficients are intrinsically dependent on the fact that the material is in powder form. An independent determination of the parameter set for a given powder would be a formidable task, as it is generally not possible to focus on a single physical property without the need to consider the effect of other parameters. Quite generally, what is done in the literature relies on a single macroscopic experiment to calibrate a simulation parameter, assuming rather arbitrarily the effect of the others to be limited. Such an approach was followed for instance by Meier et al.[30], who used Angle of Repose (AOR) data to determine the effective surface energy (γ). However, a limitation of this approach is that it is necessary first to know rolling friction coefficient (μ_{ro}) to accurately determine γ [40]. Therefore, the approach of the present paper is to conduct a sensitivity analysis on a wide parameter range to identify general trends on the relative influence of contact law parameters.

2.3.1. *Effective surface energy*

The drop test method developed by Zafar et al. allows measurement of the effective surface energy of a particle [28]. Drop test is based on equilibrium between JKR pull-off force shown in Eq. (10) [27] and particle deceleration force due to an impact. Nan et al.[19] determined this value at 9 mJ/m^2 for 316L powder. However, this value cannot be directly used, due to the Young's Modulus reduction, mentioned above. Indeed, despite an unchanged pull-off force from a physical standpoint, adhesion work would numerically increase because of the larger overlapping allowed by softer particles. Eq. (11) shows the scaling law between surface energy and Young's modulus [41, 42]. The initial value of 9 mJ/m^2 is scaled to 0.5 mJ/m^2 by using a simulation Young's modulus equal to 0.2 GPa.

$$\overrightarrow{F_{n,\text{pull-off}}} = -3/2\ \pi\gamma R^* \tag{10}$$

$$\gamma_{\text{simu}} = \gamma_{\text{exp}} \left(\frac{E_{\text{simu}}}{E_{\text{exp}}} \right)^{2/5} \tag{11}$$

In the present work, surface energy varies between 0 and 1 mJ/m^2. This large interval allows coverage of studies ignoring adhesion [43, 44] up to the higher value found in the literature for 316L powder [45]. Interestingly, most of studies describing the same issue use a surface energy with an order of magnitude of 0.1 mJ/m^2 by taking into account the Eq. (11) [19, 46, 47].

2.3.2. *Sliding friction coefficient*

Sliding friction coefficient can be influenced by particles' surface roughness. As explained by Shaheen et al.[47], the increase of surface roughness will cause a reduction of the contact area. Thus, normal pressure will increase for a given

contact force. Plastic deformation is then possible, increasing tangential force before sliding. Yim et al.[20] confirmed this assumption by calibrating two powders with different roughness. Roughness was measured by Atomic Force Microscopy. Then, DEM parameters were calibrated by static and dynamic Angle of Repose. Another approach consists in the gluing of powder on a substrate, which allows direct measurement of sliding friction, because particles cannot roll. Friction can be implemented against a substrate, e.g. a plate manufactured by powder bed fusion [19, 48] or against a similarly glued powder [31]. Slope between normal F_{T} and tangential forces F_{N} is obtained by measuring an angle of sliding with different applied weights [19, 48] or tangential force [31]. In principle, the particle sliding coefficient is equal to the global sliding coefficient of the experiment ($F_{\mathrm{N}}/F_{\mathrm{T}}$) and can be used directly as μ_{sl} [31, 48]. In the present work, tested sliding friction coefficients range in the interval [0.2, 1.2] as proposed in the literature [21, 29, 48, 49].

2.3.3. Rolling friction coefficient

Rolling friction is known to be highly dependent on particle morphology [47]. It can be measured from the travel distance of a particle rolling on a plane [40]. However, such a travel distance measurement does not work for highly non-spherical particles from Water Atomization (WA) processes because of the incapacity of those particles to roll [50]. For non-cohesive powder, rolling friction can be calibrated from the Angle of Repose [50]. From automated image analyzer, rolling friction coefficient can be computed using powder eccentricity [50–52].

To account for the dependence of rolling friction on particle morphology, polygonal particles can be represented in 2D simulation by round particles with a rolling friction coefficient linked to the number of sides n_s of polygons [33]:

$$\mu_{\mathrm{ro}}^{\mathrm{estrada}} = (1/4)\tan(\pi/2n_s) \tag{12}$$

Here, the tested rolling friction coefficients are [0,0.01,0.05,0.2]. By considering the above formula, they would correspond to a perfect circle and polygons with respectively 40, 8 and 2.3 sides. The last value has of course no physical meaning but it is proposed to model a highly non-spherical powder like water-atomized powder.

In the literature, rolling friction coefficients are often set between 0.005 and 0.1 [14, 20, 21, 48]. Sometimes rolling resistance is ignored, which corresponds to a zero rolling friction coefficient [15].

2.3.4. Restitution coefficient

Restitution coefficient is defined as the ratio of the particle velocity after and before a collision [26]. In practice, it can be measured following the impact of particles on a plane with a high-speed camera. Nan et al. measured a restitution coefficient for 316L powder of 0.64 ± 0.084 [19]. In order to investigate restitution coefficient (e) effects, four values were tested in the [0.1,0.9] range, such a large interval comprising most of the values used in the literature for metallic or polymeric materials [13, 21, 29, 46, 47, 49]. In most DEM parameters sensitivity analysis, e is assumed not to have a real impact and kept fixed between 0.3 and 0.9 [30, 47, 53]; moreover, it could be reduced to 0.1 to stabilize the simulation [49].

2.3.5. Variation range

To sum things up, all reference parameters for contact laws are chosen according to values given in the literature. Variation ranges are wide in order to cover many different values used in literature. All reference parameters (fixed and modified) as well as variation range are presented in Table 3. Parameters are

first changed for all contact types simultaneously (results referred to *all* contact types in the following). However, since as mentioned before contact parameters between two powder particles or between a powder particle and the plate or blade are expected to be different, they will also be modified independently for each contact type. In that case, when a parameter is modified, all others are kept identical to their reference value, and the results will be presented as *powder/powder (po/po)* and *powder/plate (po/pl)* contact.

For surface energy simulations, we only considered *po/po* contact. It may appear a priori surprising to neglect powder adhesion on blade and plate, but when the present work was initiated, the MUSEN software did not allow non-zero surface energy for these contacts. We thus decided to proceed modeling only *powder/powder* adhesion. Fortunately, when updates of MUSEN were afterwards implemented, it was checked on a number of test cases that the results were not significantly modified when accounting for powder blade and powder plate adhesion. In any case, the conclusions drawn in the manuscript can be expected to hold. Sliding and rolling friction parameters will be first modified for all contact types at the same time (*all*). Then, the ones that are more influential will be modified independently for *powder/powder* (*po/po*) and *powder/plate* (*po/pl*) contact. Finally, the contact parameters between powder and blade are not investigated because the study of the effect of blade geometry is, as mentioned earlier, beyond the scope of this work [10, 12, 14].

2.4. Powder bed characterization

2.4.1. Height and density

In powder bed fusion process, powder bed density, height and roughness are key descriptors of powder bed quality and used by most authors [10, 15, 17, 21, 47]. In addition, in an L-PBF configuration, segregation could lead to differential laser interaction as a function of the horizontal position over the powder bed. It

Table 3. Reference powder parameters and variation range.

Parameter	Symbol	Reference value	Variation range
Young's Modulus (Pa)	E	$2 * 10^8$	–
Particle density (kg/m^3)	ρ	7900	–
Poisson's ratio	ν	0.3	–
Effective surface energy (mJ/m^2)	γ	0.5 [19]	[0; 1] [21, 43]
Sliding friction coefficient	μ_{sl}	0.7 [46]	[0.2; 1.2] [29, 48]
Rolling friction coefficient	μ_{ro}	0.05 [47]	[0; 0.2] [15, 20]
Restitution coefficient	e	0.6 [19, 21]	[0.1; 0.9] [23, 49]

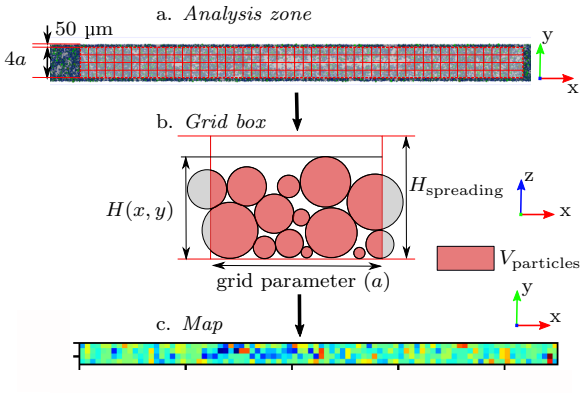

Fig. 3. Powder bed analysis with grid for height and density.

could create molten pool heterogeneity and then pores [10]. For this study, our choice is to measure powder bed density, height and segregation.

Height and density analysis routine used here is inspired by the work of Meier et al.[15]. First, the bed is voxelized at a resolution of 1 micrometer. Then, a grid presented in Fig. 3 with a 100 µm parameter (a) is selected to consider only significant variations. Indeed, a typical laser spot diameter used in L-PBF is 100 µm, and besides such a 100 µm grid parameter is sufficiently large to encompass a statistically relevant number of particles. The 50 µm margin on each side

avoids numerical artifacts from periodic boundaries.

Density and height are determined on each grid box. Local height $H(x, y)$ is the maximum value for a box as seen in Fig. 3(b). Local box density $\varphi(x, y)$ is defined as the volume occupied by particles over the complete box volume calculated with $H(x, y)$ as height as seen in Eq.(13). Using local height $H(x, y)$ allows the removal of the height effect on density values. For boxes where height is zero, a situation met when no particles are in the box, the density is fixed to 0. Then, height and density averages ($\bar{H}$ and $\bar{\varphi}$) are computed as well as standard deviations over all boxes.

$$\varphi(x, y) = \frac{V_{\text{particles}}(x, y)}{a^2 H(x, y)} \tag{13}$$

2.4.2. Segregation

Segregation is a known phenomenon in granular systems and experimentally observed in the powder bed spreading process [9]. Segregation occurs when particles composing a granular media have different properties like size, shape or density [54]. In our case, only size differentiates particles. Percolation-mechanisms can be invoked to explain size segregation. Thanks to gravity, small particles move through voids kept between large particles [55]. A consequence on powder bed spreading is the preferential deposition of small particles in the first section of the bed [10]. As a matter of fact, DEM allowed the confirmation of percolation-induced segregation during powder spreading [21]. To quantify segregation, the volume moment mean diameter D_{43} is calculated all along the bed inside fixed length divisions. It is computed from particle radius as follows in Eq. (14); it is the average diameter weighted by volume.

$$D_{43} = 2 \left(\sum_i {R_i}^4 \; / \; \sum_i R_i^3 \right) \tag{14}$$

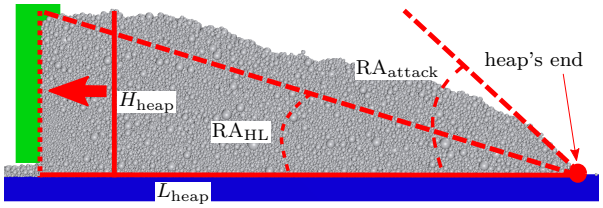

Fig. 4. Recoating Angles description: RA_{HL} and $\text{RA}_{\text{attack}}$.

2.5. Powder heap characterization

In this study, the powder heap is characterized by two Recoating Angles (RA). Indeed, a simple fitting of the heap top surface, as done by Chen et al.[23], is not possible because of the complex observed heap shapes. We thus decided to define both a global and a local RA, both angles being represented in Fig. 4. A global heap angle called RA_{HL} is derived using the height H_{heap} and the length (L_{heap}) of the powder heap:

$$RA_{\text{HL}} = \arctan\left(H_{\text{heap}}/L_{\text{heap}}\right) \tag{15}$$

The local Angle of attack $\text{RA}_{\text{attack}}$ corresponds to the angle at the end of the powder heap, where the end of the heap is identified as the first point without powder from the blade. To define this angle, a moving average of the heap height along x-axis first smooths the heap surface. The nominal half-width of the moving average is arbitrarily fixed to 200 µm, except near the end of the heap where it is adaptative. Then, the $\text{RA}_{\text{attack}}$ is the maximum slope angle calculated between two points separated by the previous half-width.

3. Results

3.1. Numerical standard deviation

In order to estimate relevant error bars on the results that will be discussed, it appeared interesting to run identical simulations to check the reproducibility of the observed results. Indeed, starting from an exactly identical generation, tiny iterative numerical discrepancies over the 10^8 time steps occurring during a simulation are likely to come to slight different results. In addition, slightly different initial conditions (see particle generation procedure) can also lead to deviations. In order to quantify these mechanisms, 3 runs of simulation with reference powder parameters introduced in Table 3 were first done using the same initial state of the particles (REF,REF1,REF2). In addition, to evaluate the deviation due to the slight variation within the initial state, 2 more simulations are run from different initial particle generations keeping the same generation box, porosity and PSD (REFA,REFB). Then, particles are randomly packed running from scratch the same filling algorithm, but with same specifications.

At first, slight but significant differences are observed: for instance, an isolated elongated empty patch, due to a particle larger than the gap in front of the blade, is well visible on Fig. 5(a). This large particle was blocked for some time, preventing flow and deposition of particles. After some millimeters, this particle is finally set free, releasing particle flow. This particle crossing the blade gap briefly increases forces measured on the blade by 2 orders of magnitude. Interestingly, for exactly the same initial conditions, the REF1 and REF2 runs also exhibit elongated empty patches but at different locations, meaning that small iterative discrepancies have to be involved. However, elongated empty patches are not observed on runs REFA and REFB, meaning that slight differences in terms of particle generation may have a significant effect.

Table A.1 in the appendix details the density, height and RA results as well as

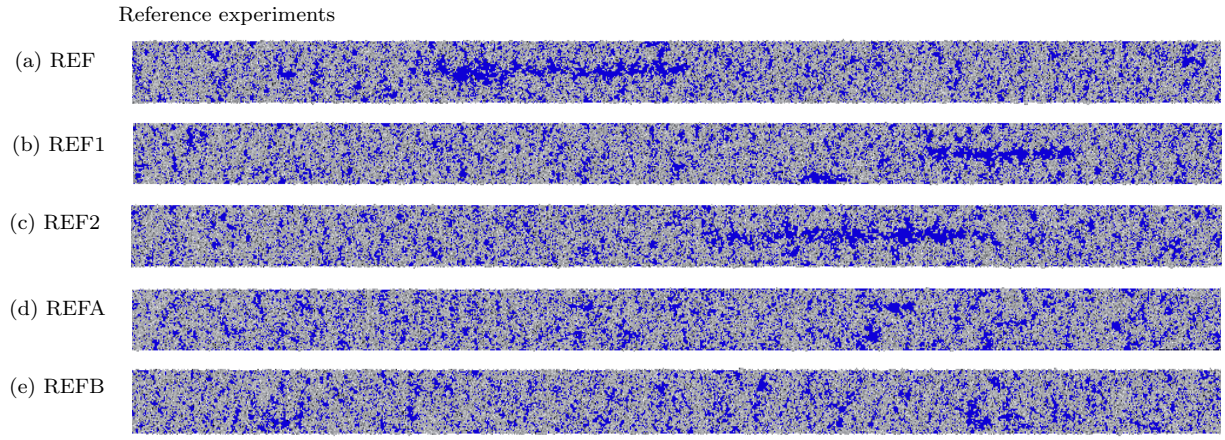

Fig. 5. Raw powder beds from different reference simulations. The plate is blue and particles are gray.

average and standard deviation over those 5 simulations. Fortunately, the above mentioned differences do not translate to very large variations when analyzed on a statistical basis. Anticipating the results to be presented below, the error bars corresponding to the standard deviations observed on those 5 spreadings will be seen to be quite low compared to variations due to contact law sensitivity. In the following, when comparison is made to a reference, the REF simulation serves as the basis.

3.2. Overview of the powder bed

Turning to the effect of contact law parameters, a first overview on simulations carried out changing all contacts simultaneously is shown in Fig. 6. It allows the visualization of some important phenomena that will be discussed later on. More generally, it is worth stating that isolated empty patches previously discussed for the reference bed are observed on many high quality continuous beds because of particles larger than the gap, as visible in Fig. 6(a,b,i). Despite an overall satisfactory quality of the powder bed, larger particles may occasionally stay jammed because of their size.

A high surface energy leads to empty patches larger than 100 µm, see Fig. 6(d). Therefore, some boxes of the grid will be empty, meaning a larger variation of height and density along the bed. A low sliding friction coefficient does not allow particles to stick on the plate; it results in no powder deposition, see Fig. 6(e). High rolling resistance creates many small empty patches uniformly distributed on bed, see Fig. 6(j). Qualitatively, the higher the sliding friction and the lower the rolling friction, the better the homogeneity of the powder bed.

3.3. Height and density

Bed height and density results are presented in Fig. 7. Mean height and density ($\bar{H}$ and $\bar{\varphi}$) are plotted against the various parameters. In addition, as mentioned above, sliding and rolling friction coefficients are modified independently for each contact type. Effects of *powder/powder* (*po/po*), *powder/plate* (*po/pl*) and *all* contacts parameters are respectively plotted in red, blue and green. Let us also recall that for surface energy simulations, we only considered *po/po* contacts.

3.3.1. Spreading length effect

For the 30 mm bed, the blind length L_{blind} is unchanged. However, the analysis zone is 15 mm longer. The measured height and density of the 30 mm bed are not very different when compared to the 15 mm length simulations. This therefore supports our assumption that 15 mm is long enough to be representative of the powder deposition in terms of height and density.

3.3.2. Effective surface energy effect

In order to quantify the effect of effective surface energy, powder parameters are kept to their reference values except γ, which is equal to $[0, 0.25, 0.5, 0.75, 1]$. Effect on mean height and density are shown in Fig. 7(a and e). For surface energy under 0.5 mJ/m^2, the mean height ($\bar{H}$) is not significantly affected staying

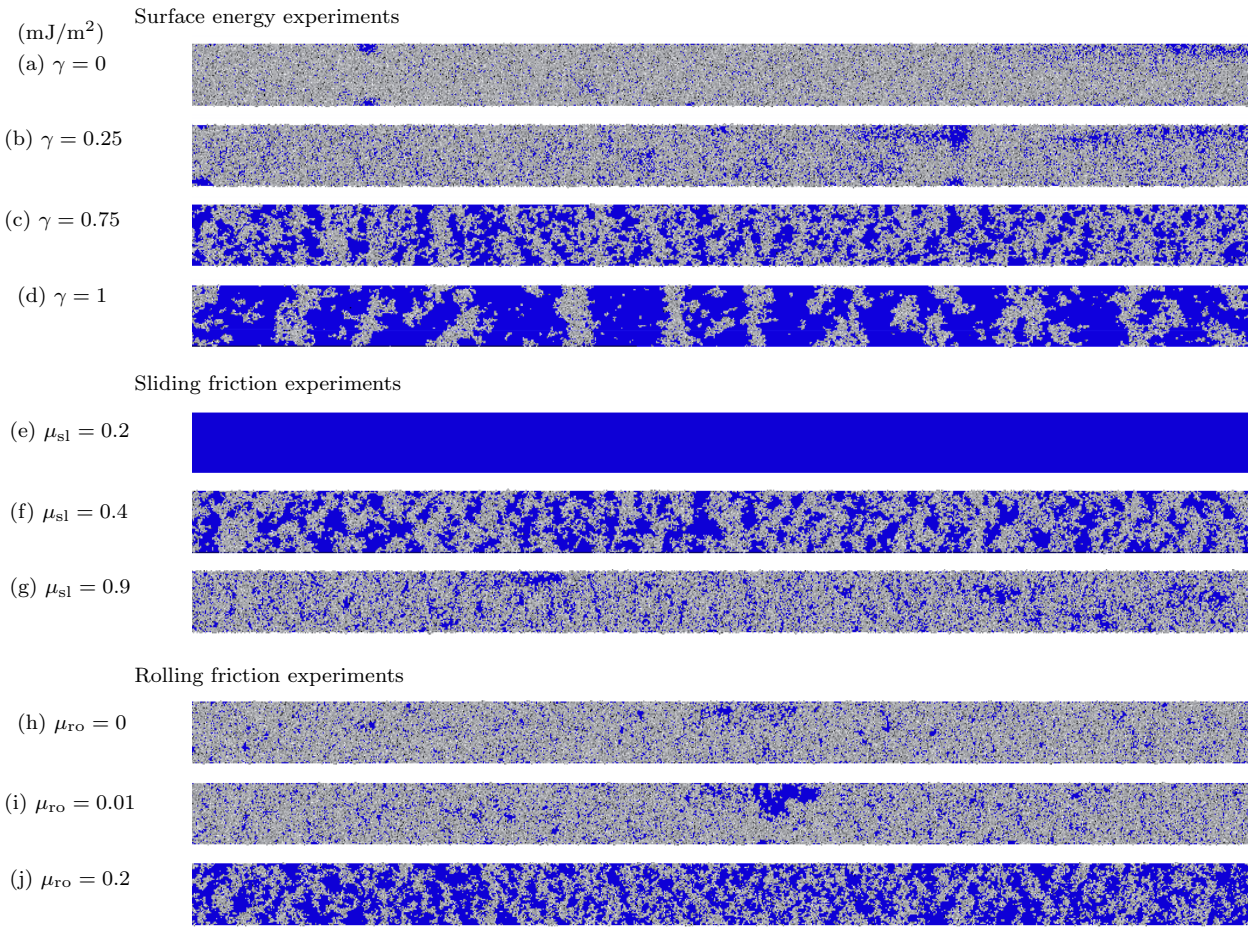

Fig. 6. Raw powder beds from different simulations with different coefficient values. Only *powder/powder* contacts are modified for surface energy simulations. For sliding and rolling friction coefficients, all contact types are modified.

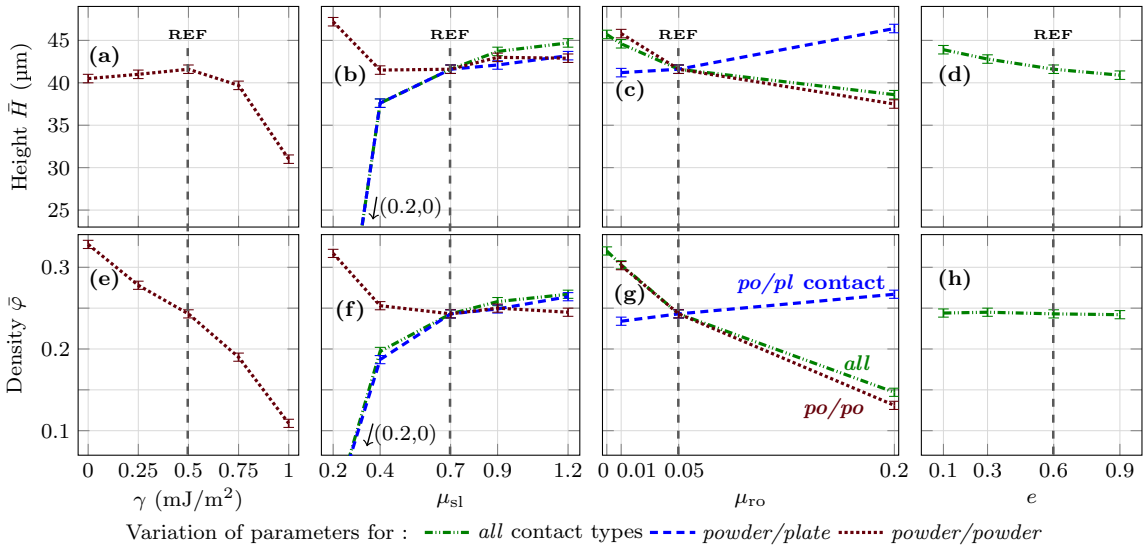

Fig. 7. Effects of surface energy, sliding, rolling and restitution coefficients on mean spread height ($\bar{H}$) and density ($\bar{\varphi}$).

around 2/3 of $H_{\text{spreading}}$. On the other hand, the mean density ($\bar{\varphi}$) is linearly affected in the all range going from 0.33 for $\gamma = 0$ mJ/m^2 to 0.11 for $\gamma = 1$ mJ/m^2. The height and density variations along the powder bed barely exceed the scatter observed on reference experiments.

Bed is denser and smoother for γ values less than 0.5 mJ/m^2. Between 0.5 and 1 mJ/m^2 mean density and height jointly decrease, whereas deviations increase. The density standard deviation over grid boxes takes values closes to the mean density ($\bar{\varphi}$) whereas the height standard deviation reaches half-mean height ($\bar{H}/2$), a situation characteristic of a poor bed quality with large voids zones. When the effective surface energy takes values between 0.75 and 1 mJ/m^2, the powder bed will become irregular with empty grid boxes as visible in Fig. 6(d). Those empty patches are the worst situation for powder melting. This result confirms the predominance of the surface energy effect according to previously published studies [15, 47].

3.3.3. Sliding friction effect

Results are shown in Fig. 7(b and f). First, we consider the friction coefficient to be the same for all contacts (i.e. *po/po*, *po/pl* as well as *powder/blade* contacts): it is denoted $\mu_{\mathrm{sl},all}$. Over $\mu_{\mathrm{sl},all} = 0.7$ a quasi plateau is observed for density ($\bar{\varphi} = 25\%$) and height ($\bar{H} = 2/3\ H_{\mathrm{spreading}}$). For $\mu_{\mathrm{sl},all}$ lower than 0.7 a powder bed degradation is observed until that powder is totally pushed out the plate when $\mu_{\mathrm{sl},all} = 0.2$. For $\mu_{\mathrm{sl},all} = 0.4$, the decreases are about 10% from the plateau value for the height and about 25% for the density.

Interestingly, modifying the sliding friction coefficient only for contacts between powder and plate leads to the same results. Sliding friction coefficient between powder and plate appears to be a key material parameter. A sliding friction around 0.4 with plate is required for the plate to hold the powder particles and achieve a satisfactorily spreading powder.

Moreover, a *powder/powder* sliding friction ($\mu_{\mathrm{sl},po/po}$) ranging from 0.4 to 1.2 shows no effect, suggesting a powder displacement by rolling. When the sliding friction coefficient with plate is large enough, a low sliding friction between powder particles (see $\mu_{\mathrm{sl},po/po} = 0.2$ case) improves mean height by 15% and density by 25%. Powder displacement by sliding is probably allowed in that case.

3.3.4. Rolling friction effect

As for the sliding friction coefficient, the effect of the rolling friction (μ_{ro}) was studied on *all*, *po/po* and *po/pl* contact types. Firstly, as seen in Fig. 7(c and g), height and density are continuously affected in the whole range of $\mu_{\mathrm{ro},all}$, going from 0.33 to 0.15 for density and from 45 µm to 38 µm for height. However height and density variation along bed remain limited compared to the case of high surface energy (1 $\mathrm{mJ/m^2}$) simulation.

A modification of only the *powder/powder* rolling friction coefficient ($\mu_{\mathrm{ro},po/po}$)

amplifies the variation already observed for $\mu_{\mathrm{ro},all}$. Collective behavior is then essentially governed by *powder/powder* contacts. This suggests that spreading a powder that rolls with difficulty, such as water atomized powder for example, would lead to looser but continuous beds that could potentially fulfill the requirements for an L-PBF process.

On the other hand, an increase of the *powder/plate* rolling friction coefficient ($\mu_{\mathrm{ro},po/pl}$) is beneficial for bed quality. For instance a value of $\mu_{\mathrm{ro},po/pl} = 0.2$ improves both density and height by 10% compared to the reference value.

3.3.5. Restitution coefficient

As seen in Fig. 7(d and h), the variation of the restitution coefficient between 0.1 and 0.9 has a negligible impact. Our conclusion is that, at least for our process conditions, its determination is not an issue in this interval for powder spreading experiment.

3.4. Segregation

3.4.1. Powder parameters effects

From now on, since it will be seen that most relevant segregation phenomena take place within the first few millimeters, the analysis zone will start at the very beginning of the building plate. In other words, as opposed to what was done previously, we will not consider a blind zone from the feeding plate. The volume moment mean diameter of particles D_{43} along the powder bed is plotted in Fig. 8. All parameter sets lead to the preferential deposition of smaller particles at the beginning of spreading. In the first 3 millimeters of the powder bed, D_{43} approximately increases from 70% to 85% of its initial value (19.8 µm) as calculated from the starting powder characteristics. Then, the mean volume diameter reaches a plateau at 90% to 95% of this initial value.

Starting with surface energy, it is seen that segregation is not very sensitive to the value of γ. Only at a zero surface energy a somewhat smaller D_{43} on

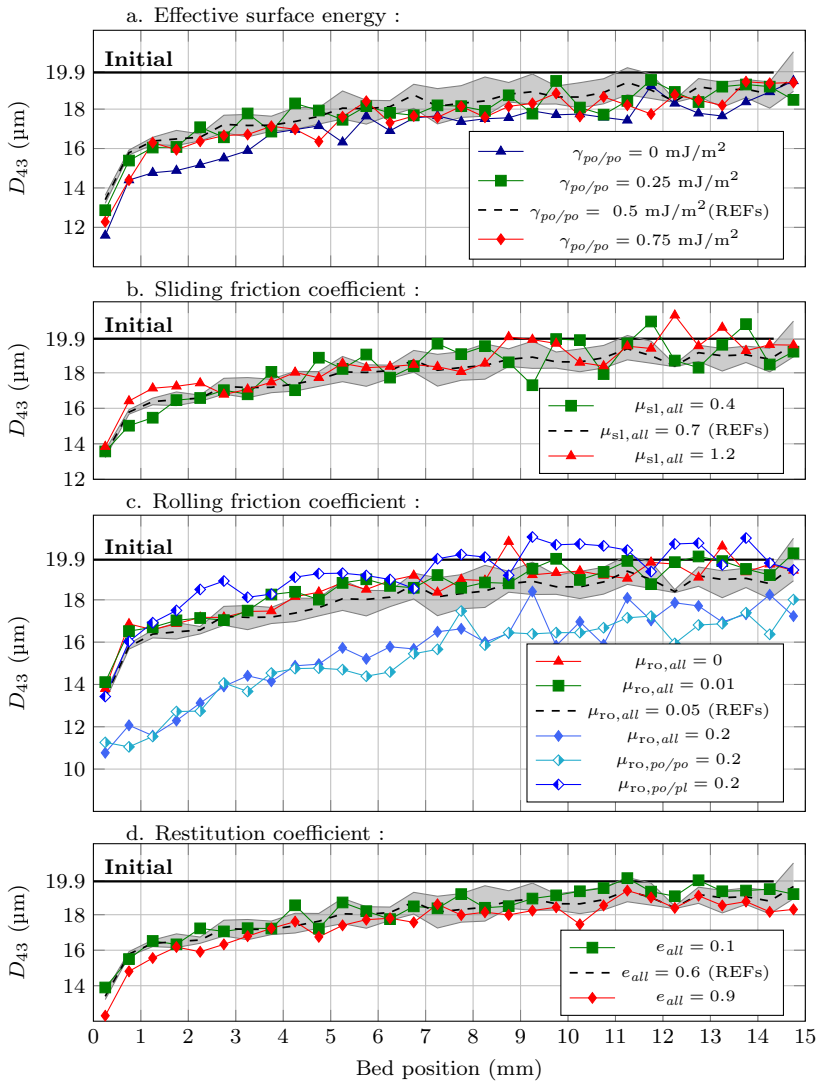

Fig. 8. Volume moment mean diameter D_{43} along powder bed for different simulations. Bed is divided in 30 boxes of 500 µm long. The dashed line and the gray shaded zone respectively represent the average and the minimum-maximum spread for the 5 simulations with reference parameters (REFs).

the first 4 mm of the bed can be observed. This can be interpreted stating that without adhesion, smallest particles are free to move between larger ones. The simulation with the effective surface energy equal to 1 mJ/m^2 is not plotted. As mentioned earlier, the powder bed presents large empty patches visible in Fig. 6(d) which make the curve chaotic. Moreover, in this case segregation can be considered a minor issue compared the voids that plague bed quality.

As observed for surface energy, the effect of sliding and restitution coefficients on segregation is quite limited. Regarding rolling friction, a high coefficient ($\mu_{\mathrm{ro},all} = 0.2$) leads to the largest segregation. D_{43} is initially smaller than for other simulations at the beginning of deposition. In addition, the increase is slower leading to a significant and continuous evolution until half of the bed length. Then, it stabilizes around 85% of the initial value. The effect of the rolling coefficient is again due to *powder/powder* contacts. Indeed, curves for *all* and *po/po* contacts are nearly overlapped.

To sum things up on segregation issues, since the observed variations take place within the first few millimeters of the building plates where parts are rarely positioned in practice, it can be stated that segregation should not be a critical issue, at least for spherical powders from a gas atomization process. On the other hand, less spherical particles from a water atomization process with a higher rolling friction coefficient could segregate on longer distances and potentially induce variations of the received laser power which could be an issue for part manufacturing.

3.4.2. Spreading length effect

As done in Fig. 8, Fig. 9 shows the effect of the spreading length on segregation. Two spreads of 15 mm and 30 mm length in REF conditions are represented, where the volume moment mean diameter of particles D_{43} is plotted as a function of either bed length in mm or bed length fraction (normalized

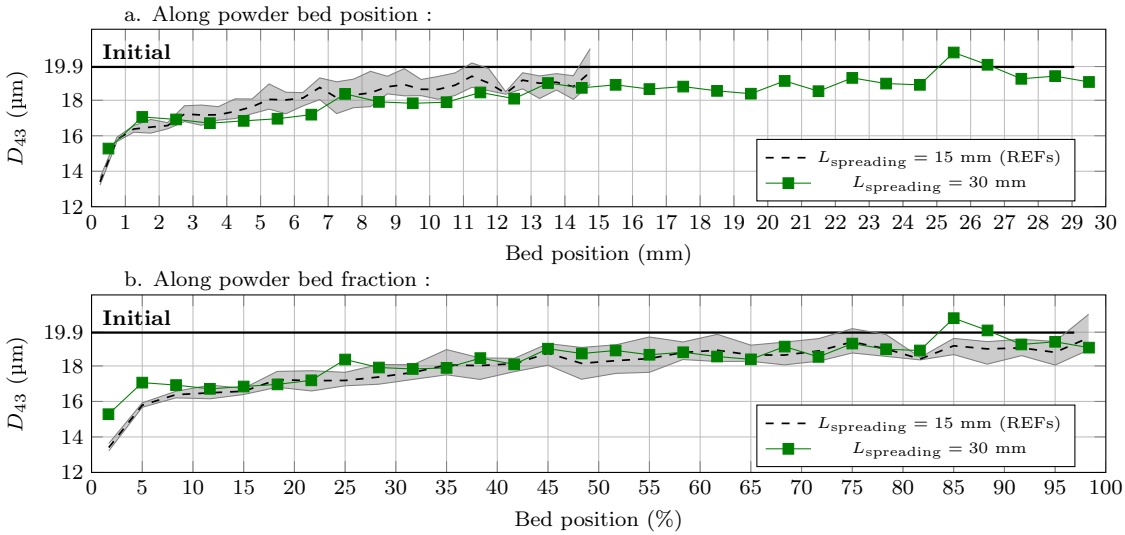

Fig. 9. Volume moment mean diameter D_{43} along powder beds for reference parameter set with two spreading lengths. a/ Diameter is plotted along powder bed position, each box is 500 µm long. b/ Diameter is plotted along powder bed fraction, bed is divided into 30 boxes. The dashed line and the gray shaded zone respectively represent the average and the minimum-maximum spread for the 5 simulations with reference parameters (REFs).

by spreading length). During the first 3 mm, D_{43} curves overlap when using the bed length in mm as x-axis. On the other hand, after these first 3 mm, curves overlap when using the bed length fraction as the x-axis. Interestingly, the Root Mean Square Deviation RMSD between 15 mm and 30 mm geometries is reduced by considering fractions instead of lengths. The rate of reduction is between 13% and 55% for different reference simulations. Apart from the first few millimeters of spreading, this points to a better physical description of the segregation phenomena using normalized spreading lengths.

3.5. Recoating Angles (RA)

3.5.1. RA stability along spreading

Heap profile evolves during spreading. RA_{attack} and RA_{HL} are respectively plotted in the Fig. 10(a and b) all along spreading process for reference parameter simulations as well as for the 30 mm geometry simulation. The insert of Fig. 10 enlightens the effect of particle ejections that take place in the vicinity of the heap's front end. Our moving average procedure (see Fig. 4) then fails, leading to outlier points that were removed from the RAs calculation. RA_{HL} is seen to increase in a linear manner. Therefore, a linear regression is implemented to characterize the evolution of this angle. The data from the 15 mm and 30 mm do not overlap, meaning that the measured slope is depending on the quantity of powder involved. However, the 15 mm and 30 mm data reach a similar value at the final spreading length. Then, for further comparisons of parameter sets results, RA_{HL} is characterized by the intercept value of the linear regression taken at 100% of the spreading length. It has to be noted that this observation is likely due to our choice of simulation conditions with feeding length equal to spreading length, but we nevertheless consider this value fit for comparison purposes.

RA_{attack} presents a fast increase at the beginning of the building plate. After

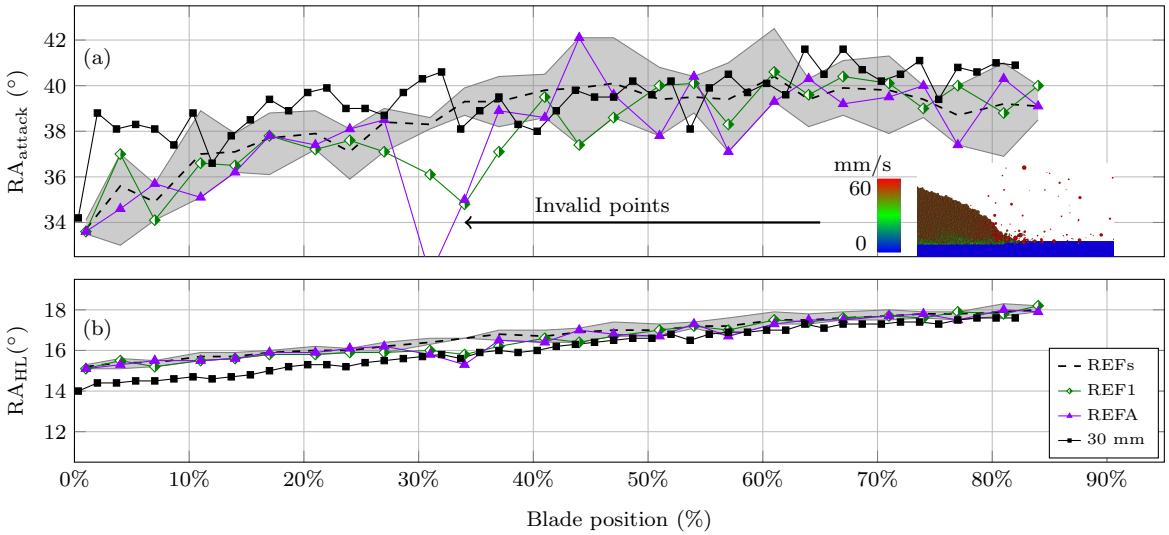

Fig. 10. RA_{attack} and RA_{HL} along bed for reference simulations. The dashed line and the gray shaded zone respectively represent the average and the minimum-maximum spread for the 5 simulations with reference parameters (REFs). Invalid points between 31% and 38% for REF1 and REFA are removed from average, min and max calculations.

the first millimeters, RA_{attack} no longer increases, but it is still subjected to significant variations. Beyond 20% of the powder bed, average and standard deviation of the RA_{attack} are 39.2° and 1.2° for reference simulations. RA_{attack} is roughly the same between both 15 mm and 30 mm geometries over 20% of the spreading length.

The RA_{attack} relative standard deviation around its mean value is 3% after the first 20% of spreading length, whereas for RA_{HL} it is about 1% around the fitting line. The higher value in the case of RA_{attack} is likely due to the fact that this indicator is sensitive to a powder behavior at the end of the heap involving only some hundreds of flowing particles in the avalanche zone. Avalanche is not continuous and subject to accelerations and decelerations, leading to strong RA_{attack} variations during spreading. On the other hand, the RA_{HL} involves powder rearrangement at the scale of the whole heap; it is less sensitive to individual events compared to RA_{attack}. Therefore, RA_{attack} and RA_{HL} can be considered as complementary indicators to characterize the heap profile.

3.5.2. Powder parameters effects

RA sensitivity analysis results are presented in Fig. 11 following the same rules used for height and density in Fig. 7. Both Recoating Angles (RA_{attack}, RA_{HL}) are plotted for all simulations. Variations of each powder parameter around reference value are plotted. Sliding and rolling friction coefficients are differentiated between *powder/powder* and *powder/plate* contacts.

To compare different parameter sets together, the heap profile is measured at 6 times locations between $t = 600$ ms and $t = 850$ ms. Those time steps are uniformly distributed between 0% and 84% of the blade displacement on the building plate as presented by Fig. 10. Our choice is made to avoid end effects on the comparison between parameter sets as the heap can be considered to be in a transient state before 17%. The spread associated to the above sampling is

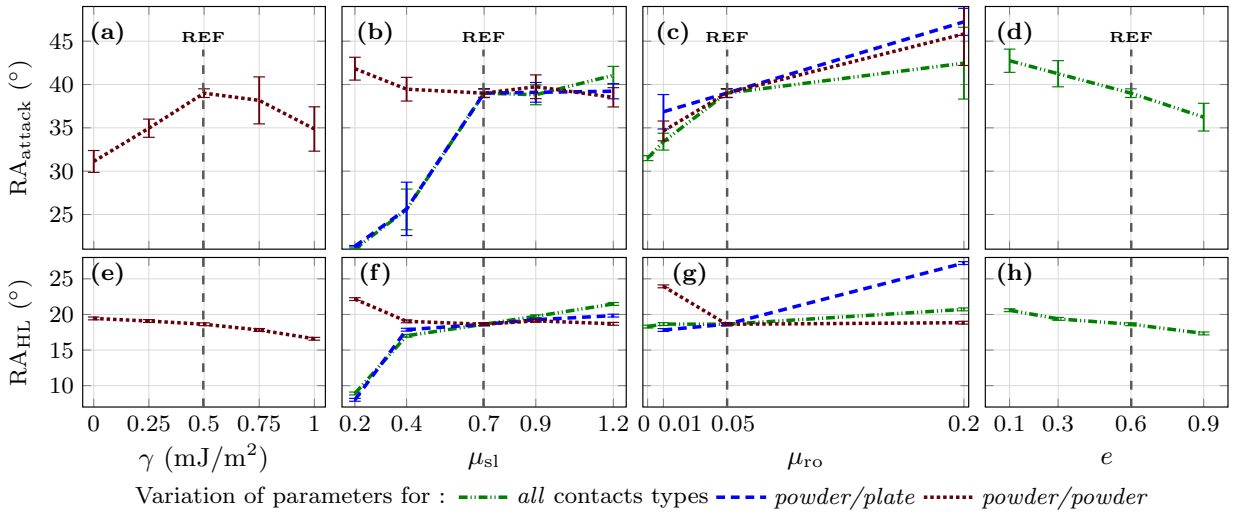

Fig. 11. Effects of surface energy, sliding, rolling and restitution coefficient on both definitions of RAs.

less than 1° for $\mathrm{RA_{attack}}$, and less than 0.2° for $\mathrm{RA_{HL}}$.

The error bars on the figure correspond to the standard deviation calculated on those 6 points for each simulation. It should be noted that when considering the whole set of reference simulations, the observed spread is equivalent.

As seen in Fig. 11, almost all simulations lead to similar effects on $\mathrm{RA_{attack}}$ and $\mathrm{RA_{HL}}$. Starting from the restitution coefficient, a larger value of e amounts to increased particle velocities after collisions, and thus to a facilitated rearrangement of the heap by particle flow. Therefore, both angles are smallest for $e = 0.9$.

Sliding friction coefficient μ_{sl} has an impact for *powder/plate* contact type as for height and density analysis. *All* and *powder/plate* contact types points again overlap. An insufficient sliding friction coefficient between powder and plate leads to low $\mathrm{RA_{attack}}$ and $\mathrm{RA_{HL}}$. Forces between plate and heap are not large enough to raise the powder heap upwards on the blade.

According to Fig. 11(g), the rolling friction coefficient has no impact on $\mathrm{RA_{HL}}$

for the *all* contact types configuration. However, each contact type has his own effect. Reducing $\mu_{\mathrm{ro},po/po}$ will reduce internal forces inside powder, facilitating the raise of the heap on the blade and thus higher $\mathrm{RA_{HL}}$. On the other hand, reducing $\mu_{\mathrm{ro},po/pl}$ facilitates powder rolling on plate. Therefore, the heap stretches, and the $\mathrm{RA_{HL}}$ is smaller. $\mathrm{RA_{attack}}$ is reduced when rolling friction is reduced for *powder/powder* contacts as well as for *powder/plate*.

The effective surface energy has a slight effect on $\mathrm{RA_{HL}}$, an increase of γ leads to a moderate decrease of $\mathrm{RA_{HL}}$. Regarding $\mathrm{RA_{attack}}$, a maximum value is observed for 0.5 $\mathrm{mJ/m^2}$. The bell-shaped curve results from a change in flow regime around 0.5 $\mathrm{mJ/m^2}$. All these results will now be discussed with a focus on particle velocities that will allow a better understanding of the involved physical phenomena.

3.6. Powder flow zones

Regarding the norm of linear velocity, different flow zones can be identified in powder heaps presented in Fig. 12, as were first observed by Zhang et al. and Yim et al.[10, 20]. First, it can be seen that most of the particles are in the quasi-static zone, where their velocities are close to that of the blade velocity, namely 50 mm/s, color code in gray in the figure. In addition, particle motion can also be characterized by their rolling velocities measured on their surfaces as characterized by Eq. (16). In the quasi-static zone, the rolling velocity of those particles, in blue in Fig. 13, is almost zero, further supporting the assumption of quasi-static behavior according in the blade frame of reference.

$$\vec{v}_{\mathrm{s},i} = \vec{\omega_i} R_i \tag{16}$$

The second zone is the free-flowing zone, also called avalanche zone [10, 20]. It is composed by particles with color code in red in front of the bed, with linear

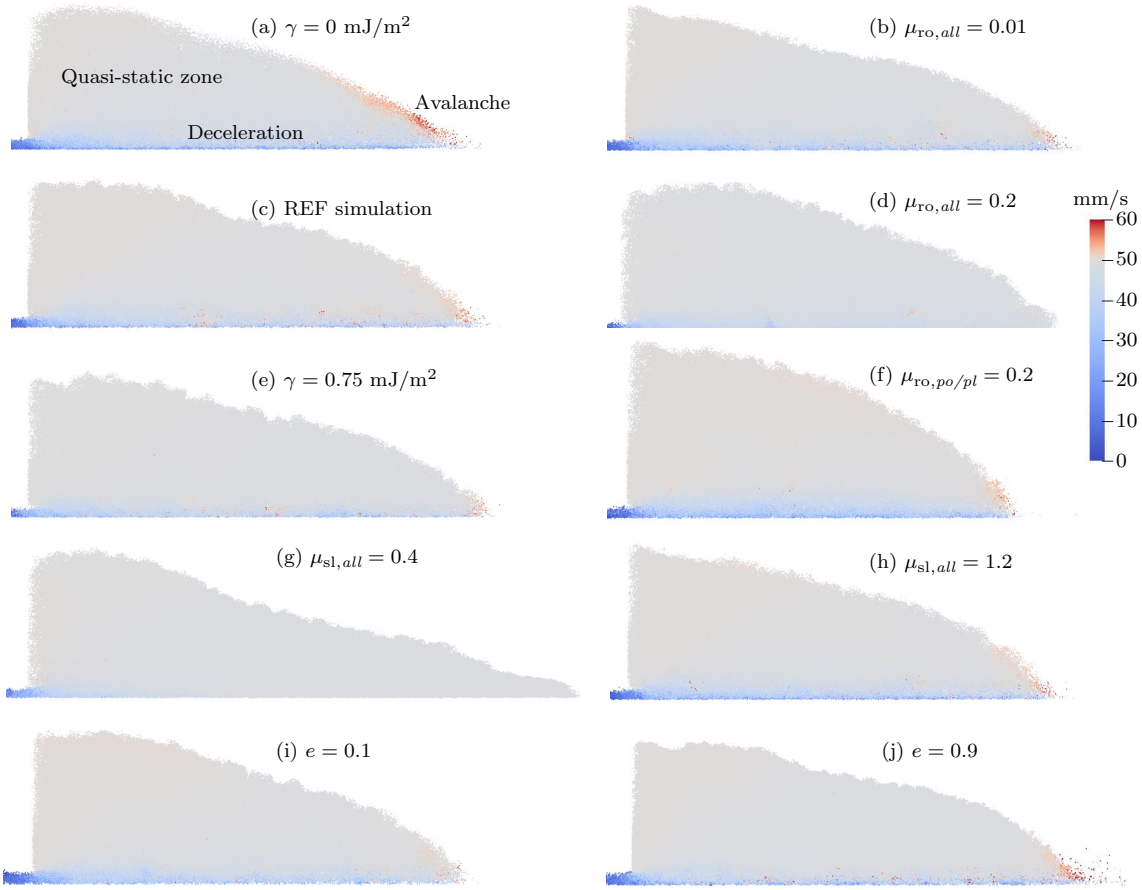

Fig. 12. Linear velocity of particles in the building plate frame, $t = 750$ ms. Each simulation is specified. Different flowing zones can be identified, particles moving at blade velocity (50 mm/s) are in the quasi-static zone. Particles faster than blade are in the avalanche zone. Then, particles slower are in the deceleration zone.

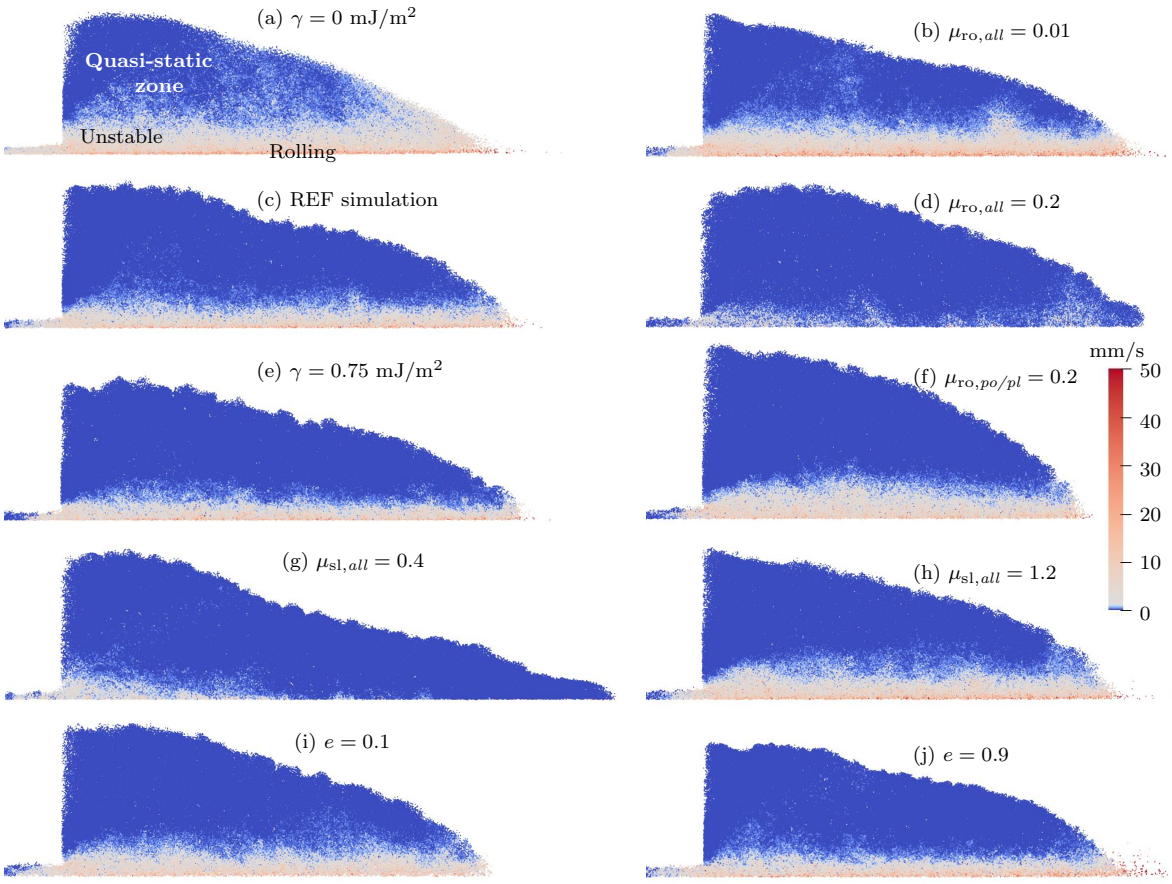

Fig. 13. Surface velocity $||\vec{v_s}||$ of particles, $t = 750$ ms. Each simulation is specified. Different flowing zones can be identified, particles with no surface velocity are in the quasi-static zone. Particles presenting a non null surface velocity, approximately between 1 and 10 mm/s, are in the unstable zone. Then, a thin rolling band is composed of particles with an high surface velocity over 20 mm/s.

velocities higher than the blade-spreading rate (see Fig. 12). Interestingly, this zone is not observed for all parameter sets, as its existence requires a sufficient powder flowability combined with a sufficiently raised upward heap. This last assumption is illustrated by the case $\mu_{\mathrm{sl},all} = 0.4$, where the plate friction is too small, resulting in a heap that is not raised upwards enough at the front of the bed. Therefore, the slope necessary for powder avalanche is too small, and particles do not fall.

The last zone is characterized by the deceleration of particles in the vicinity of the plate, with linear velocities smaller than the one of the blade (see color code blue in Fig. 12). An interesting finding of our simulations is that this zone extends all along the powder heap for favorable spreading conditions. In such cases, a specific behavior can be identified in the immediate vicinity of the plate, where the linear and surface velocities of the particles are similar, taking values between 20 and 40 mm/s and indicating a perfect rolling of the particles appears on the plate surface. Furthermore, above the building plate, powder instability extends for hundreds of micrometers along the vertical axis, translating to surface velocities between 1 and 10 mm/s (see Fig. 13). The extension of this instability zone depends on the interactions within the powder heap. For unfavorable powder spreading (e.g. in cases $\mu_{\mathrm{sl},all} = 0.4$ or $\mu_{\mathrm{ro},all} = 0.2$, particle deceleration takes place only in the vicinity (say first hundreds of micrometers) of the blade and without easy rolling on plate. This final deceleration just before passing through blade gap is probably due to shear stress created by the blade as described by Yim et al.[20]. In any case, it appears that the extent of this deceleration zone can be a good predictor of bed quality. Finally, even though outside the scope of the present work, it can be stated that improving the shear stress distribution in this ultimate deceleration zone could be achieved by optimizing the blade geometry [12, 13].

All contact law parameters are seen to modify powder flow in a specific way. On the one hand, a high effective surface energy limits the extension of powder instability over the deceleration zone, increasing the size of the quasi-static zone. On the other hand, a zero effective surface energy leads to a large deceleration zone.

The restitution coefficient does not significantly modify the deceleration zone, even if tiny red dots are visible within the deceleration zone in Fig. 12(j) for $e = 0.9$, representative of some bouncing contacts and interactions between particles. Moreover, those bouncing contacts favor particle flow, as seen at the front of the heap in the avalanche zone.

Sliding and rolling friction coefficients play a key role on the velocity profile in the deceleration zone. A low sliding friction coefficient prevents particles from rolling, the same observation being made for $\mu_{\mathrm{ro},all} = 0.2$ albeit with a different heap profile. A low rolling friction coefficient or a high sliding friction coefficient do the opposite, a more visible rolling layer can be observed as a red line, e.g. in Fig. 13(b). Nevertheless, this effect is more visible with low rolling coefficient. The case $\mu_{\mathrm{ro},po/pl} = 0.2$ is peculiar, as particles stop rolling on the plate, see Fig. 13(f), but deceleration remains nevertheless possible as seen in Fig. 12(f). There is a significant extension of the unstable zone over the deceleration area showing a good particle flow over a high friction plate.

4. Discussion

4.1. Towards an optimum heap profile for good powder bed quality

Powder bed quality thus seems to be governed by the particle behavior within the deceleration zone above the build plate. More precisely, a large deceleration zone with rolling particles is seen to be correlated with a good powder bed quality in terms of height and density. Moreover, it appears that the heap profile

is controlled by powder behavior within the deceleration and avalanche zones. First, friction with the plate leads to an upward motion of the powder heap and an increase of the RA_{HL}. Then, powder can freely flow if heap is sufficiently raised upward, creating the avalanche.

The avalanche itself is characterized by the RA_{attack}, which depends on powder properties, especially surface energy and rolling friction. Those parameters are also paramount for standard angle of repose experiments [30, 40], suggesting similar mechanisms. However, it should be noted that the RA_{attack} has no meaning if there is no avalanche zone, i.e. when particles do not flow. From the different characteristics of the powder heap, a global and a local angle of attack, it seems possible to foresee final bed quality.

In this respect, the perfect heap has a maximum RA_{HL} - characteristic of a high interaction with the plate - and a minimum RA_{attack} - characteristic of easy flowing powder. A maximal RA_{HL} with minimal RA_{attack} corresponds to a right-angled triangle, with the hypotenuse being the heap top surface. Simulations with $\gamma = 0$ mJ/m^2 or $\mu_{ro,all} = 0.01$ shown in Fig. 12(a and b) approach this perfect shape. They have a small RA_{attack} and a high RA_{HL} as seen in Fig. 11. In addition, they present ones of the best bed height and density of the analysis (see Fig. 7).

4.2. Where does segregation take place?

The detailed study of flow phenomena within the heap also allows the issue of the origin of segregation to be addressed. Indeed, segregation observed in Fig. 8 can be accounted for invoking a differential velocity between small and large particles, which results in a mean height, characterized as the average position along z-axis, lower for small particles than for large particles. Accordingly, Fig. 14 and Fig. 15 show respectively the mean velocity along z-axis and the mean height for the smallest (below D10) and the largest (above D90) particles

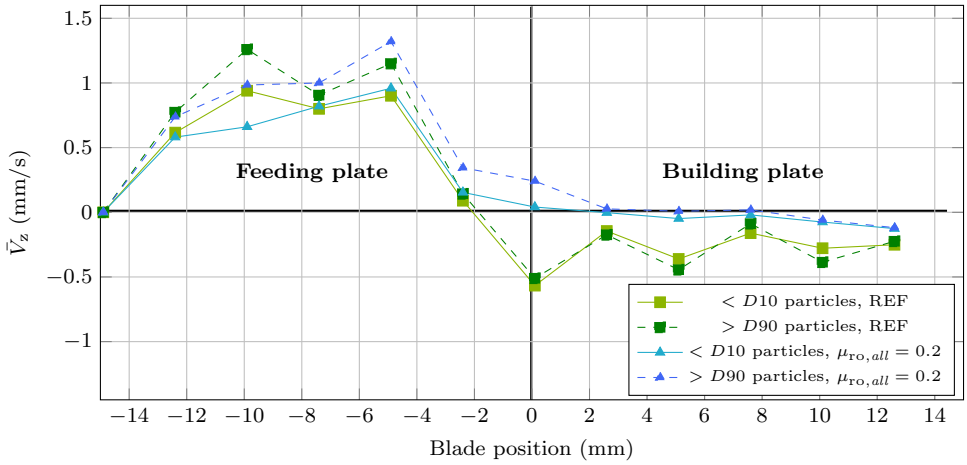

Fig. 14. Mean particle velocity along z-axis during blade movement, including powder feeding and spreading. Velocities are plotted for particles smaller than D10 and larger than D90.

within the heap during the spreading process for the reference powder parameter set and a high rolling friction case.

During powder feeding between -15 and 0 mm, the blade gathers particles on the feeding plate and pushes them frontward to form a powder heap. The vertical mean velocity $\bar{V}_z$ is positive for both large and small particles corresponding to the heap formation, but with a large speed difference between smallest and largest particles. Thus, as seen in Fig. 15, the mean height of all particles increases but more for the largest particles, inducing segregation.

Both plotted simulations show a similar behavior during feeding. The first difference that can be observed between the reference (REF) and the high rolling resistance ($\mu_{\mathrm{ro},all} = 0.2$) simulations is from -2 and 0 mm, a region corresponding to the transition between the feeding and the building plate, where there is a step of spreading height. In this region, the drop in vertical velocity is much higher for both size classes in the REF simulation, down to negative values.

In the powder spreading zone from 0 to 15 mm, starting from the REF

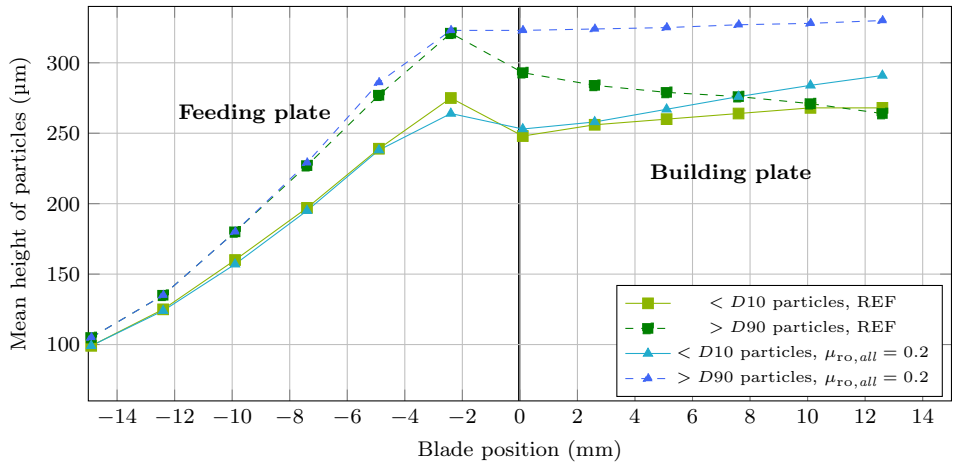

Fig. 15. Mean particle position along z-axis during blade movement, including powder feeding and spreading. Positions are plotted for particles smaller than D10 and larger than D90.

simulation, all particle velocities are nearly the same and negative as visible in Fig. 14. However, the particles mean heights move in different ways (see Fig. 15): upwards for the smallest particles and downwards for the largest. To account for such a finding, let us notice that small particles, which are initially segregated at the bottom of the heap, are deposited first. Thus, their mean height increases because particles in the bed are ousted from the average calculation. At the end of the building plate, the heap is well mixed for REF simulation. Indeed, mean heights for largest and smallest particles are nearly the same.

As for the spreading behavior in the high rolling resistance simulation $\mu_{\mathrm{ro},all} = 0.2$, particle velocity remains just below zero from 0 to 15 mm, contrary to reference simulation that exhibited significantly lower values. This is a result of a reduced powder flow for the high rolling resistance simulation. In that case, there is an increase in mean position even for the large particles during spreading. It results in a higher mean position along z-axis for all particles, and a segregated powder heap at the end of spreading as opposed to the reference case.

5. Conclusion

In this work, the effect of contact law parameters on powder spreading is numerically investigated using DEM simulations. Regarding powder bed quality, the effective surface energy is the most important contact law parameter. Its variation between 0 and 1 mJ/m^2 leads to a linear reduction of the density by a factor of more than 2; in addition, discontinuous powder bed are observed for values over 0.75 mJ/m^2. For a meaningful simulation of actual powder spreading, an accurate determination of its value is paramount. The impact of the rolling friction coefficient is also paramount for contacts between powder particles. In the tested range, μ_{ro} impact is of the same order than for surface energy. Its determination should thus be carried out using characterization techniques involving only powder particles. On the other hand, the impact of the sliding friction coefficient is more important for contacts between powder and building plate than between powder particles. Its characterization should be done for this contact type, confirming the validity of the approach of Nan et al.[19]. A minimal value of sliding friction around 0.4 with the plate is necessary in order to deposit the powder on plate. Finally, the restitution coefficient does not have a significant impact on powder bed quality; its determination is not a first order issue.

As for heap characterization, the three flowing zones identified in previous works [10, 20] were indeed observed in our simulations. But we showed that, depending on the contact law parameters, the avalanche and deceleration zones do not always exist. The deceleration zone is where the plate slows powder particles by friction, its presence is essential for adequate powder deposition. Therefore, in the case of simple geometries where the blade has no significant compaction effect, a characterization of this zone of friction between powder and plate looks essential. Interestingly, our work allows to make a connection

between bed quality and heap shape.

The effect of geometry was also verified by doubling the simulation length, which was seen to lead to insignificant variation in terms of height and density. As for particle flow within the heap, the doubling of the simulation length leads to small differences on particle size segregation and RA. Our simulations showed that the mechanisms leading to size segregation on the building plate have their origin in flow phenomena occurring during the formation of the heap on the feeding plate. This issue is therefore highly dependent on the simulation choices and the modeled geometry.

These findings can further enhance characterization protocols of AM powders in order to determine the ability of a given powder to be properly spread on a given surface, namely in terms of powder flowability and plate friction. As for perspectives, the present work points to the necessity of adequately characterizing the spreading conditions. As such, studies of deposition on an actual solidified part, as opposed to a bare plate, would be of interest. More precisely, a characterization of the rolling friction coefficient between powder and a solidified part is still unexplored and looks as essential for the simulations' accuracy. Further works on the ability of the heap shape to predict spreading quality through the identification of new descriptors should also be carried out. Finally, our methodology could be extended to include the effect of different spreading devices, e.g. blades of various shapes and orientations, as well as rollers.

6. Acknowledgments

The author gratefully acknowledge the financial support of the CEA internal program Focus Jumeau Numérique.

Appendix A.

Table A.1. Deviation tests results for height, density and Recoating Angles.

Simulation	$\bar{H}$ μm	$\bar{\varphi}$	RA_{attack}	RA_{HL}
REF	41.6	0.243	39.0°	18.6°
REF1	42.5	0.243	39.5°	18.8°
REF2	41.8	0.242	38.6°	18.9°
REFA	42.3	0.249	38.5°	18.4°
REFB	42.0	0.252	39.7°	18.7°
Estimation of the results deviations between REF, REF1, REF2, REFA and REFB :				
Mean Value	42,0	0,246	39.1°	18.7°
Standard deviation	0,4	$4 * 10^{-3}$	0.5°	0.2°
Relative standard deviation	0.9 %	1.8 %	1.5 %	1.1 %

References

[1] P. Avrampos, G.-C. Vosniakos, A review of powder deposition in additive manufacturing by powder bed fusion, Journal of Manufacturing Processes 74 (2022) 332–352. doi:10.1016/j.jmapro.2021.12.021.
URL https://www.sciencedirect.com/science/article/pii/S1526612521009002

[2] M. Lupo, D. Barletta, D. Sofia, M. Poletto, Calibration of dem for cohesive particles in the sls powder spreading process, Processes 9 (2021) 1715. doi:10.3390/pr9101715.

[3] M. Ziaee, N. B. Crane, Binder jetting: A review of process, materials, and methods, Additive Manufacturing 28 (2019) 781–801. doi:10.1016/j.addma.2019.05.031.
URL https://www.sciencedirect.com/science/article/pii/S2214860418310078

[4] M. Soulier, D. Vincent, S. Cayre, P. Faucherand, J. Bancillon, R. Laucournet, Study of 316L stainless steel powders specifications on parts printed by laser- powered - powder bed fusion (PBF), in: Conference paper Euro PM, 2018.

[5] L. Haferkamp, L. Haudenschild, A. Spierings, K. Wegener, K. Riener, S. Ziegelmeier, G. J. Leichtfried, The Influence of Particle Shape, Powder Flowability, and Powder Layer Density on Part Density in Laser Powder Bed Fusion, Metals 11 (3) (2021) 418. doi:10.3390/met11030418.
URL https://www.mdpi.com/2075-4701/11/3/418

[6] M. J. Matthews, G. Guss, S. A. Khairallah, A. M. Rubenchik, P. J. Depond, W. E. King, Denudation of metal powder layers in laser

812 powder bed fusion processes, Acta Materialia 114 (2016) 33–42.
813 doi:10.1016/j.actamat.2016.05.017.
814 URL https://www.sciencedirect.com/science/article/pii/
815 S135964541630355X

816 [7] Y. Ma, T. M. Evans, N. Philips, N. Cunningham, Numerical sim-
817 ulation of the effect of fine fraction on the flowability of powders
818 in additive manufacturing, Powder Technology 360 (2020) 608–621.
819 doi:10.1016/j.powtec.2019.10.041.
820 URL https://www.sciencedirect.com/science/article/pii/
821 S0032591019308642

822 [8] D. Ruggi, M. Lupo, D. Sofia, C. Barrès, D. Barletta, M. Poletto, Flow
823 properties of polymeric powders for selective laser sintering, Powder
824 Technology 370 (2020) 288–297. doi:10.1016/j.powtec.2020.05.069.
825 URL https://www.sciencedirect.com/science/article/pii/
826 S0032591020304435

827 [9] A. Mussatto, R. Groarke, A. O'Neill, M. A. Obeidi, Y. Delaure,
828 D. Brabazon, Influences of powder morphology and spreading param-
829 eters on the powder bed topography uniformity in powder bed fusion
830 metal additive manufacturing, Additive Manufacturing 38 (2021) 101807.
831 doi:10.1016/j.addma.2020.101807.
832 URL https://www.sciencedirect.com/science/article/pii/
833 S2214860420311799

834 [10] J. Zhang, Y. Tan, X. Xiao, S. Jiang, Comparison of roller-
835 spreading and blade-spreading processes in powder-bed additive
836 manufacturing by DEM simulations, Particuology 66 (2022) 48–58.
837 doi:10.1016/j.partic.2021.07.005.

URL https://www.sciencedirect.com/science/article/pii/S1674200121001474

[11] J. Zhang, Y. Tan, T. Bao, Y. Xu, X. Xiao, S. Jiang, Discrete Element Simulation of the Effect of Roller-Spreading Parameters on Powder-Bed Density in Additive Manufacturing, Materials 13 (10) (2020) 2285, number: 10 Publisher: Multidisciplinary Digital Publishing Institute. doi:10.3390/ma13102285.
URL https://www.mdpi.com/1996-1944/13/10/2285

[12] T. Cheng, H. Chen, Q. Teng, Q. Wei, In-situ experiment tests and particulate simulations on powder paving process of additive manufacturing, Particuology 74 (2023) 164–172. doi:10.1016/j.partic.2022.07.001.
URL https://linkinghub.elsevier.com/retrieve/pii/S1674200122001274

[13] S. Haeri, Optimisation of blade type spreaders for powder bed preparation in Additive Manufacturing using DEM simulations, Powder Technology 321 (2017) 94–104. doi:10.1016/j.powtec.2017.08.011.
URL https://www.sciencedirect.com/science/article/pii/S0032591017306551

[14] L. Wang, A. Yu, E. Li, H. Shen, Z. Zhou, Effects of spreader geometry on powder spreading process in powder bed additive manufacturing, Powder Technology 384 (2021) 211–222. doi:10.1016/j.powtec.2021.02.022.
URL https://linkinghub.elsevier.com/retrieve/pii/S003259102100125X

[15] C. Meier, R. Weissbach, J. Weinberg, W. A. Wall, A. J. Hart, Critical influences of particle size and adhesion on the powder layer uniformity in metal additive manufacturing, Journal of Materials Processing Technology

266 (2019) 484–501. doi:10.1016/j.jmatprotec.2018.10.037.
URL https://www.sciencedirect.com/science/article/pii/S0924013618304801

[16] H. Chen, T. Cheng, Z. Li, Q. Wei, W. Yan, Is high-speed powder spreading really unfavourable for the part quality of laser powder bed fusion additive manufacturing?, Acta Materialia 231 (2022) 117901. doi:10.1016/j.actamat.2022.117901.
URL https://www.sciencedirect.com/science/article/pii/S1359645422002865

[17] J. Wang, D. Yao, M. Li, X. An, S. Li, W. Hou, X. Zhang, G. Yang, J. Wang, L. Wang, Hierarchical effects of multi-layer powder spreading in the electron beam powder bed fusion additive manufacturing of pure tungsten material, Additive Manufacturing 55 (2022) 102835. doi:10.1016/j.addma.2022.102835.
URL https://www.sciencedirect.com/science/article/pii/S2214860422002342

[18] F. Dubois, F. Radjaï, Discrete-Element Modeling of Granular Materials, farhang radjaï and frédéric dubois Edition, ISTE & WILEY, 2011.

[19] W. Nan, M. Pasha, T. Bonakdar, A. Lopez, U. Zafar, S. Nadimi, M. Ghadiri, Jamming during particle spreading in additive manufacturing, Powder Technology 338 (2018) 253–262. doi:10.1016/j.powtec.2018.07.030.
URL https://linkinghub.elsevier.com/retrieve/pii/S0032591018305278

[20] S. Yim, H. Bian, K. Aoyagi, K. Yamanaka, A. Chiba, Spreading behavior of Ti48Al2Cr2Nb powders in powder bed fusion additive manufacturing process: Experimental and discrete element method study, Additive

Manufacturing (2021) 102489doi:10.1016/j.addma.2021.102489.
URL https://www.sciencedirect.com/science/article/pii/S2214860421006370

[21] D. Yao, J. Wang, M. Li, T. Zhao, Y. Cai, X. An, R. Zou, H. Zhang, H. Fu, X. Yang, Q. Zou, Segregation of 316L stainless steel powder during spreading in selective laser melting based additive manufacturing, Powder Technology (2022) 117096doi:10.1016/j.powtec.2021.117096.
URL https://linkinghub.elsevier.com/retrieve/pii/S0032591021011141

[22] Z. Snow, R. Martukanitz, S. Joshi, On the development of powder spreadability metrics and feedstock requirements for powder bed fusion additive manufacturing, Additive Manufacturing 28 (2019) 78–86. doi:10.1016/j.addma.2019.04.017.
URL https://linkinghub.elsevier.com/retrieve/pii/S2214860418309941

[23] H. Chen, Q. Wei, S. Wen, Z. Li, Y. Shi, Flow behavior of powder particles in layering process of selective laser melting: Numerical modeling and experimental verification based on discrete element method, International Journal of Machine Tools and Manufacture 123 (2017) 146–159. doi:10.1016/j.ijmachtools.2017.08.004.
URL https://linkinghub.elsevier.com/retrieve/pii/S089069551730130X

[24] L. I. Escano, N. D. Parab, L. Xiong, Q. Guo, C. Zhao, K. Fezzaa, W. Everhart, T. Sun, L. Chen, Revealing particle-scale powder spreading dynamics in powder-bed-based additive manufacturing process by high-speed x-ray

915 imaging, Sci Rep 8 (1) (2018) 15079. doi:10.1038/s41598-018-33376-0.
916 URL https://www.nature.com/articles/s41598-018-33376-0

917 [25] H. Hertz, Ueber die Berührung fester elastischer Körper, Journal fur die
918 Reine und Angewandte Mathematik 1882 (92) (1882) 156–171. doi:10.
919 1515/crll.1882.92.156.

920 [26] Y. Tsuji, T. Tanaka, T. Ishida, Lagrangian numerical simulation of plug
921 flow of cohesionless particles in a horizontal pipe, Powder Technology 71 (3)
922 (1992) 239–250. doi:10.1016/0032-5910(92)88030-L.
923 URL https://www.sciencedirect.com/science/article/pii/
924 003259109288030L

925 [27] K. L. Johnson, K. Kendall, A. D. Roberts, Surface energy and the con-
926 tact of elastic solids, Proc. R. Soc. Lond. A 324 (1558) (1971) 301–313.
927 doi:10.1098/rspa.1971.0141.
928 URL https://royalsocietypublishing.org/doi/10.1098/rspa.1971.
929 0141

930 [28] U. Zafar, C. Hare, A. Hassanpour, M. Ghadiri, Drop test: A new method
931 to measure the particle adhesion force, Powder Technology 264 (2014)
932 236–241. doi:10.1016/j.powtec.2014.04.022.
933 URL https://www.sciencedirect.com/science/article/pii/
934 S0032591014003283

935 [29] L. Wang, E. L. Li, H. Shen, R. P. Zou, A. B. Yu, Z. Y. Zhou, Adhesion
936 effects on spreading of metal powders in selective laser melting, Powder
937 Technology 363 (2020) 602–610. doi:10.1016/j.powtec.2019.12.048.
938 URL https://www.sciencedirect.com/science/article/pii/
939 S0032591019311532

[30] C. Meier, R. Weissbach, J. Weinberg, W. A. Wall, A. John Hart, Modeling and characterization of cohesion in fine metal powders with a focus on additive manufacturing process simulations, Powder Technology 343 (2019) 855–866. doi:10.1016/j.powtec.2018.11.072.
URL https://linkinghub.elsevier.com/retrieve/pii/S0032591018309884

[31] A. Angus, L. A. A. Yahia, R. Maione, M. Khala, C. Hare, A. Ozel, R. Ocone, Calibrating friction coefficients in discrete element method simulations with shear-cell experiments, Powder Technology 372 (2020) 290–304. doi:10.1016/j.powtec.2020.05.079.
URL https://www.sciencedirect.com/science/article/pii/S0032591020304538

[32] P. S. Desai, A. Mehta, P. S. M. Dougherty, C. F. Higgs, A rheometry based calibration of a first-order DEM model to generate virtual avatars of metal Additive Manufacturing (AM) powders, Powder Technology 342 (2019) 441–456. doi:10.1016/j.powtec.2018.09.047.
URL https://www.sciencedirect.com/science/article/pii/S0032591018307587

[33] N. Estrada, E. Azéma, F. Radjai, A. Taboada, Identification of rolling resistance as a shape parameter in sheared granular media, Phys. Rev. E 84 (1) (2011) 011306, publisher: American Physical Society. doi:10.1103/PhysRevE.84.011306.
URL https://link.aps.org/doi/10.1103/PhysRevE.84.011306

[34] M. Dosta, V. Skorych, MUSEN: An open-source framework for GPU-accelerated DEM simulations, SoftwareX 12 (2020) 100618. doi:10.1016/j.softx.2020.100618.

URL https://www.sciencedirect.com/science/article/pii/S2352711020303319

[35] P. A. Cundall, O. D. L. Strack, A discrete numerical model for granular assemblies, Géotechnique 29 (1) (1979) 47–65, publisher: ICE Publishing. doi:10.1680/geot.1979.29.1.47.
URL https://www.icevirtuallibrary.com/doi/abs/10.1680/geot.1979.29.1.47

[36] M. Soulier, A. Burr, N. Dubois, G. Roux, J. Maisonneuve, R. Laucournet, Analytical and numerical modelling of stainless steel powders spreading in powder-bed processes for additive manufacturing, 2021, cited by: 1.
URL https://www.scopus.com/inward/record.uri?eid=2-s2.0-85149183116&partnerID=40&md5=d0020592471e27fc86eff64946575849

[37] N. J. Brown, J.-F. Chen, J. Y. Ooi, A bond model for DEM simulation of cementitious materials and deformable structures, Granular Matter 16 (3) (2014) 299–311. doi:10.1007/s10035-014-0494-4.
URL https://doi.org/10.1007/s10035-014-0494-4

[38] M. Paulick, M. Morgeneyer, A. Kwade, Review on the influence of elastic particle properties on DEM simulation results, Powder Technology 283 (2015) 66–76. doi:10.1016/j.powtec.2015.03.040.
URL https://www.sciencedirect.com/science/article/pii/S0032591015002533

[39] H. Chen, Y. G. Xiao, Y. L. Liu, Y. S. Shi, Effect of Young's modulus on DEM results regarding transverse mixing of particles within a rotating drum, Powder Technology 318 (2017) 507–517. doi:10.1016/j.powtec.2017.05.047.

URL https://www.sciencedirect.com/science/article/pii/S0032591017304540

[40] Y. C. Zhou, B. D. Wright, R. Y. Yang, B. H. Xu, A. B. Yu, Rolling friction in the dynamic simulation of sandpile formation, Physica A: Statistical Mechanics and its Applications 269 (2) (1999) 536–553. doi:10.1016/S0378-4371(99)00183-1.
URL https://www.sciencedirect.com/science/article/pii/S0378437199001831

[41] J. Hærvig, U. Kleinhans, C. Wieland, H. Spliethoff, A. L. Jensen, K. Sørensen, T. J. Condra, On the adhesive JKR contact and rolling models for reduced particle stiffness discrete element simulations, Powder Technology 319 (2017) 472–482. doi:10.1016/j.powtec.2017.07.006.
URL https://www.sciencedirect.com/science/article/pii/S0032591017305430

[42] K. Washino, E. L. Chan, T. Tanaka, DEM with attraction forces using reduced particle stiffness, Powder Technology 325 (2018) 202–208. doi:10.1016/j.powtec.2017.11.024.
URL https://www.sciencedirect.com/science/article/pii/S0032591017308938

[43] Y. M. Fouda, A. E. Bayly, A DEM study of powder spreading in additive layer manufacturing, Granular Matter 22 (1) (2020) 10. doi:10.1007/s10035-019-0971-x.
URL http://link.springer.com/10.1007/s10035-019-0971-x

[44] S. Haeri, Y. Wang, O. Ghita, J. Sun, Discrete element simulation and experimental study of powder spreading process in additive manufacturing, Powder Technology 306 (2017) 45–54. doi:10.1016/j.powtec.2016.11.002.

URL https://linkinghub.elsevier.com/retrieve/pii/S0032591016307720

[45] D. Yao, X. Liu, J. Wang, W. Fan, M. Li, H. Fu, H. Zhang, X. Yang, Q. Zou, X. An, Numerical insights on the spreading of practical 316 L stainless steel powder in SLM additive manufacturing, Powder Technology 390 (2021) 197–208. doi:10.1016/j.powtec.2021.05.082.
URL https://linkinghub.elsevier.com/retrieve/pii/S0032591021004915

[46] H. Chen, Q. Wei, Y. Zhang, F. Chen, Y. Shi, W. Yan, Powder-spreading mechanisms in powder-bed-based additive manufacturing: Experiments and computational modeling, Acta Materialia 179 (2019) 158–171. doi:10.1016/j.actamat.2019.08.030.
URL https://www.sciencedirect.com/science/article/pii/S1359645419305427

[47] M. Shaheen, A. Thornton, S. Luding, T. Weinhart, The influence of material and process parameters on powder spreading in additive manufacturing, Powder Technology 383 (2021) 564–583. doi:10.1016/j.powtec.2021.01.058.

[48] S. Wu, Z. Lei, M. Jiang, J. Liang, B. Li, Y. Chen, Experimental investigation and discrete element modeling for particle-scale powder spreading dynamics in powder-bed-fusion-based additive manufacturing, Powder Technology 403 (2022) 117390. doi:10.1016/j.powtec.2022.117390.
URL https://www.sciencedirect.com/science/article/pii/S0032591022002844

[49] K. Marchais, J. Girardot, C. Metton, I. Iordanoff, A 3D DEM simulation to study the influence of material and process parameters on spreading of

metallic powder in additive manufacturing, Comp. Part. Mech. 8 (4) (2021) 943–953. doi:10.1007/s40571-020-00380-z.
URL https://link.springer.com/10.1007/s40571-020-00380-z

[50] A. Tripathi, V. Kumar, A. Agarwal, A. Tripathi, S. Basu, A. Chakrabarty, S. Nag, Quantitative DEM simulation of pellet and sinter particles using rolling friction estimated from image analysis, Powder Technology 380 (2021) 288–302. doi:10.1016/j.powtec.2020.11.024.
URL https://www.sciencedirect.com/science/article/pii/S0032591020310779

[51] C. M. Wensrich, A. Katterfeld, Rolling friction as a technique for modelling particle shape in DEM, Powder Technology 217 (2012) 409–417. doi:10.1016/j.powtec.2011.10.057.
URL https://www.sciencedirect.com/science/article/pii/S0032591011006000

[52] C. M. Wensrich, A. Katterfeld, D. Sugo, Characterisation of the effects of particle shape using a normalised contact eccentricity, Granular Matter 16 (3) (2014) 327–337. doi:10.1007/s10035-013-0465-1.
URL https://doi.org/10.1007/s10035-013-0465-1

[53] Q. Wu, C. Qiao, W. Fan, Q. Zou, X. An, H. Fu, H. Zhang, X. Yang, H. Ji, S. Li, X. Zhang, L. Wang, Insights into surface chemistry induced powder layer characteristic evolutions in additive manufacturing, Powder Technology 407 (2022) 117635. doi:10.1016/j.powtec.2022.117635.
URL https://www.sciencedirect.com/science/article/pii/S0032591022005290

[54] A. Rosato, C. Windows-Yule, Segregation in Vibrated Granular Systems,

Segregation in Vibrated Granular Systems, 2020, pages: 291. doi:10.1016/B978-0-12-814199-1.00002-0.

[55] Y. Fan, K. V. Jacob, B. Freireich, R. M. Lueptow, Segregation of granular materials in bounded heap flow: A review, Powder Technology 312 (2017) 67–88. doi:10.1016/j.powtec.2017.02.026.
URL https://www.sciencedirect.com/science/article/pii/S0032591017301535